Article:

Miller, Helen Louise, Cosgrove, Jason, Wollman, Adam orcid.org/0000-0002-5501-8131 et al. (5 more authors) (2018) High-speed single-molecule tracking of CXCL13 in the B-Follicle. Frontiers in immunology. 1073. p. 1073. ISSN 1664-3224

https://doi.org/10.3389/fimmu.2018.01073

High-speed single-molecule tracking of CXCL13 in the B-Follicle

Helen Miller[1], **Jason Cosgrove**[2], **Adam Wollman**[2], **Peter O'Toole**[2], **Mark Coles**[1], **Mark C. Leake**[2*]

[1]University of Oxford, United Kingdom, [2]University of York, United Kingdom

Submitted to Journal:
Frontiers in Immunology

Specialty Section:
Cytokines and Soluble Mediators in Immunity

Article type:
Original Research Article

Manuscript ID:
355984

Received on:
26 Jan 2018

Revised on:
28 Apr 2018

Frontiers website link:
www.frontiersin.org

Conflict of interest statement

The authors declare that the research was conducted in the absence of any commercial or financial relationships that could be construed as a potential conflict of interest

Author contribution statement

H.M. built the bespoke fluorescence microscope, overseen by M.C.L.; J.C. prepared biological samples overseen by M.C.C. H.M. and J.C. performed the imaging; H.M. analyzed the data from all experiments with input from A.W., M.C.L. H.M. ran simulations of fluorescence data on code adapted from A.W. P.O.T. oversaw FCS and FRAP microscopy. H.M., A.W. prepared the figures with input from all authors. H.M., J.C, and M.C.L. wrote the manuscript with input from all authors.

Keywords

single-molecule imaging, Chemokines, Biophysics, lymphoid tissues., Single-molecule tracking

Abstract

Word count: 295

Soluble factors are an essential means of communication between cells and their environment. However, many molecules readily interact with extracellular matrix components, giving rise to multiple modes of diffusion. The molecular quantification of diffusion in situ is thus a challenging imaging frontier, requiring very high spatial and temporal resolution. Overcoming this methodological barrier is key to understanding the precise spatial patterning of the extracellular factors that regulate immune function. To address this, we have developed a high-speed light microscopy system capable of millisecond sampling in ex vivo tissue samples and sub-millisecond sampling in controlled in vitro samples to characterize molecular diffusion in a range of complex microenvironments. We demonstrate that this method outperforms competing tools for determining molecular mobility of fluorescence correlation spectroscopy (FCS) and fluorescence recovery after photobleaching (FRAP) for evaluation of diffusion. We then apply this approach to study the chemokine CXCL13, a key determinant of lymphoid tissue architecture, and B-cell mediated immunity. Super-resolution single-molecule tracking of fluorescently labeled CCL19 and CXCL13 in collagen matrix was used to assess the heterogeneity of chemokine mobility behaviors, with results indicating an immobile fraction and a mobile fraction for both molecules, with distinct diffusion rates of 8.4 ± 0.2 µm2s-1 and 6.2 ± 0.3 µm2s-1 respectively. To better understand mobility behaviors in situ we analyzed CXCL13-AF647 diffusion in murine lymph node tissue sections and observed both an immobile fraction and a mobile fraction with a diffusion coefficient of 6.6 ± 0.4 µm2s 1, suggesting that mobility within the follicle is also multimodal. In quantitatively studying mobility behaviors at the molecular level, we have obtained an increased understanding of CXCL13 bioavailability within the follicle. Our high-speed single-molecule tracking approach affords a novel perspective from which to understand the mobility of soluble factors relevant to the immune system.

Funding statement

Supported by the Biological Physical Sciences Institute (BPSI), MRC grants MR/K01580X/1 (P.O.T. and M.C.L), MC_PC_15073 (Z.Z., M.C.C. and M.C.L) and BBSRC grant BB/N006453/1 (A.J.M.W. and M.C.L.). J.C. is supported by a studentship from the Wellcome Trust 4-year PhD programme (WT095024MA): Combating Infectious Disease: Computational Approaches in Translation Science.

Ethics statements

(Authors are required to state the ethical considerations of their study in the manuscript, including for cases where the study was exempt from ethical approval procedures)

Does the study presented in the manuscript involve human or animal subjects: Yes

Please provide the complete ethics statement for your manuscript. Note that the statement will be directly added to the manuscript file for peer-review, and should include the following information:

- Full name of the ethics committee that approved the study
- Consent procedure used for human participants or for animal owners
- Any additional considerations of the study in cases where vulnerable populations were involved, for example minors, persons with disabilities or endangered animal species

As per the Frontiers authors guidelines, you are required to use the following format for statements involving human subjects: This study was carried out in accordance with the recommendations of [name of guidelines], [name of committee]. The protocol was approved by the [name of committee]. All subjects gave written informed consent in accordance with the Declaration of Helsinki.
For statements involving animal subjects, please use:
This study was carried out in accordance with the recommendations of 'name of guidelines, name of committee'. The protocol was approved by the 'name of committee'.

If the study was exempt from one or more of the above requirements, please provide a statement with the reason for the exemption(s).
Ensure that your statement is phrased in a complete way, with clear and concise sentences.

All experiments conformed to the ethical principles and guidelines approved by the University of York Institutional and Animal Care Use Committee.

High-speed single-molecule tracking of CXCL13 in the B-Follicle

Helen Miller[1,6,+], Jason Cosgrove[2,3,4+], Adam J. M. Wollman[1,3], Emily Taylor[2,3], Zhaoukun Zhou[1,3], Peter J. O' Toole[3,5], Mark C. Coles[2,3,7,*] and Mark C. Leake[1,3,*]

[1]Department of Physics
[2]Centre of Immunology and Infection
[3]Department of Biology
[4]Department of Electronics
[5]Bioscience Technology Facility
University of York, YO10 5DD, UK.
[6]Clarendon Laboratory, Department of Physics, University of Oxford, OX1 3PU, UK.
[7]Kennedy Institute of Rheumatology, University of Oxford, OX3 7FY, UK.

+ Co-first authors
* Correspondence should be addressed to M.C.L: mark.leake@york.ac.uk and M.C.C: mark.coles@kennedy.ox.ac.uk

Abstract

Soluble factors are an essential means of communication between cells and their environment. However, many molecules readily interact with extracellular matrix components, giving rise to multiple modes of diffusion. The molecular quantification of diffusion *in situ* is thus a challenging imaging frontier, requiring very high spatial and temporal resolution. Overcoming this methodological barrier is key to understanding the precise spatial patterning of the extracellular factors that regulate immune function. To address this, we have developed a high-speed light microscopy system capable of millisecond sampling in *ex vivo* tissue samples and sub-millisecond sampling in controlled *in vitro* samples to characterize molecular diffusion in a range of complex microenvironments. We demonstrate that this method outperforms competing tools for determining molecular mobility of fluorescence correlation spectroscopy (FCS) and fluorescence recovery after photobleaching (FRAP) for evaluation of diffusion. We then apply this approach to study the chemokine CXCL13, a key determinant of lymphoid tissue architecture, and B-cell mediated immunity. Super-resolution single-molecule tracking of fluorescently labeled CCL19 and CXCL13 in collagen matrix was used to assess the heterogeneity of chemokine mobility behaviors, with results indicating an immobile fraction and a mobile fraction for both molecules, with distinct diffusion rates of 8.4 ± 0.2 $\mu m^2 s^{-1}$ and 6.2 ± 0.3 $\mu m^2 s^{-1}$ respectively. To better understand mobility behaviors *in situ* we analyzed CXCL13-AF647 diffusion in murine lymph node tissue sections and observed both an immobile fraction and a mobile fraction with a diffusion coefficient of 6.6 ± 0.4 $\mu m^2 s^{-1}$, suggesting that mobility within the follicle is also multimodal. In quantitatively studying mobility behaviors at the molecular level, we have obtained an increased understanding of CXCL13 bioavailability within the follicle. Our high-speed single-molecule tracking approach affords a novel perspective from which to understand the mobility of soluble factors relevant to the immune system.

Keywords

Single-molecule imaging, single-molecule tracking, chemokines, biophysics, lymphoid tissues.

Introduction

Within the immune system, soluble factors such as chemokines, cytokines, and growth factors drive graded responses to extracellular signals, regulating processes including immune cell recruitment at sites of infection (Kienle and Lämmermann, 2016), lymphoid tissue formation (Buckley et al., 2015; Drayton et al., 2006), and the maturation of adaptive immune responses (Pereira et al., 2010). Despite their fundamental importance, the precise spatial distribution of soluble factors within tissues remains unclear, due in part to a dearth of experimental techniques capable of measuring diffusion *in situ.*

The emergence of super-resolution imaging in light microscopy has yielded significant insights into the structure and dynamics of the immune synapse (Dustin and Baldari, 2017), with the potential to elucidate the precise spatial localization of soluble factors within the context of a complex tissue. These methods enable spatial localization of single fluorescent probes more than an order of magnitude better than the standard optical resolution limit of ~250 nm, facilitating direct visualization of dynamic molecular processes. Barriers to using super-resolution for quantifying rapid molecular diffusion in biological processes in the aqueous inter- and intra-cellular regions in tissues include poor temporal resolution, due to constraints imposed from limited photon emission, and challenges in data interpretation due to heterogeneous mobility behaviors such as complex underlying diffusion modes or the presence of mixed populations of molecules in multimeric forms.

To achieve the most rapid sampling possible, traditional single-molecule fluorescence tracking techniques must compromise on the image quality or on the type of probe used. Elastic and interferometric scattering can overcome poor fluorophore photophysics to enable rapid sampling, however, they either use relatively large probes that exhibit steric hindrance, or achieve poor specificity in heterogeneous sample environments unless used in conjunction with fluorescent labeling (Andrecka et al., 2015; Fujiwara et al., 2002; Leake, 2013; Miller et al., 2018; Piliarik and Sandoghdar, 2014). Scanning fluorescence methods such as stimulated emission depletion microscopy (STED (Hell and Wichmann, 1994) are limited to ~1 Hz typical frame rates with faster imaging up to ~1,000 Hz possible by trading image quality (Schneider et al., 2015); MINFLUX imaging (Balzarotti et al., 2017) can operate at 8,000 localisations per second in bacterial cells, but only tracks one molecule at a time, while widefield approaches such as fast variants of photoactivatable localization microscopy (PALM) (Betzig et al., 2006) and stochastic optical reconstruction microscopy (STORM) (Rust et al., 2006) have integration times of on the order of tens of milliseconds for individual image frames with full reconstructions commonly taking several seconds. Structured illumination approaches (Gustafsson, 2000; Song et al., 2016) at best have frame rates of several hundred Hz and high intensity illumination methods have enabled super-resolution imaging in living cells at around millisecond timescales (Plank et al., 2009; Reyes-Lamothe et al., 2010). Sub-millisecond fluorescence imaging has been reported previously using relatively large fluorescent bead probes (Juette and Bewersdorf, 2010), tracking a single molecule at a time (Ashley et al., 2016), in plasma membranes using fluorescently labeled cholesterol analogues or Fab fragments (Hiramoto-Yamaki et al., 2014; Wieser et al., 2007) and at short distances from the coverslip using TIRF and HILO imaging (van 't Hoff et al., 2008). However, these methods encounter significant challenges in data interpretation when samples and mobility are heterogeneous, as encountered in tissues. Our method is the first, to our knowledge, to enable sub-millisecond molecular tracking using a minimally perturbative nanoscale organic dye reporter in a heterogeneous 3D aqueous environment typical of interstitial regions between cells in tissues.

Single-molecule tracking can be used to measure diffusion coefficients of proteins and molecules in localized regions and offers the opportunity to investigate the heterogeneity one molecule at a time compared to the ensemble technique of fluorescence recovery after photobleaching (FRAP) (Axelrod et al., 1976a, 1976b; Edidin et al., 1976) and quasi single-molecule approach of fluorescence correlation spectroscopy (FCS) (Ehrenberg and Rigler, 1974; Magde et al., 1972). These three techniques have been compared using proteins present in the plasma membrane of cells (Adkins et al., 2007; Calizo and Scarlata, 2013; Lagerholm et al., 2017; Macháň et al., 2016), supported lipid bilayers (Guo et al., 2008; Macháň et al., 2016), and giant unilamellar vesicles (Guo et al., 2008), which are all approximated as 2D surfaces.

In this study we use single-molecule imaging approaches to quantify the diffusion of the chemotactic cytokines (chemokines) CXCL13 and CCL19 (Fig. 1(b)). These molecules are key regulators of lymphocyte migration that are present in spatially distinct regions of the lymphoid tissues such as the lymph node (Pereira et al., 2010). Chemokines are small proteins (~10kDa) that bind G-protein Coupled Receptors (GPCRs) leading to polarization of the actomyosin cytoskeleton and directed migration along localized concentration gradients (Rot and von Andrian, 2004). Chemokine bioavailability is regulated across broad spatiotemporal scales, making direct visualization of these molecules *in situ* challenging. Chemokines are secreted within a dense, heterogeneous microenvironment and undergo transient interactions with their cognate GPCRs and components of the extracellular matrix (ECM) before undergoing receptor-mediated scavenging or enzymatic degradation (Colditz et al., 2007; Rot and von Andrian, 2004; Schulz et al., 2016). In addition, chemokines are heterogeneous in their binding affinities and are subject to multimerization effects; characteristics that may alter their mobility (Bennett et al., 2011; von Hundelshausen et al., 2017). Simplified hydrodynamic predications (Einstein, 1905) employing estimations for the Stokes radius of chemokines and the fluid environment viscosity suggest that chemokine diffusion in hypothetically homogeneous intracellular media in the absence of binding effects would be rapid at ~150 $\mu m^2/s$, implying ~50 s for a single molecule to diffuse across a 200 μm diameter region of lymphoid tissue. However, this estimate is likely to be a poor predictor of diffusivity, as it does not account for dynamic molecular interactions encountered in dense, heterogeneous tissues.

In the following sections we describe a method to overcome previous technological barriers to the study of molecular mobility *in situ*. Specifically, we have adapted a standard inverted epifluorescence microscope, making important modifications to facilitate minimally perturbative sub-millisecond single-molecule tracking of rapidly diffusing fluorescently labeled biomolecules via sub-diffraction limit localizations, and developed bespoke software for precise quantification of underlying molecular mobility of tracked particles. We compared FCS, FRAP and single molecule tracking on the well-characterized test system for molecular mobility of bovine serum albumin (BSA), labeled with Alexa Fluor 647 (AF647). We then applied our method to quantify the diffusion of CCL19 and CXCL13 (Fig. 1b), in a range of environments of increasing complexity comprising (i) buffer alone and in the presence of the highly-branched polysaccharide Ficoll to vary the fluid environment viscosity, (ii) the presence of either surface-immobilized heparan sulfate, or a collagen gel matrix, and further (iii) AF647 tagged CXCL13 was tracked in an *ex vivo* native mouse lymph node environment. Our data suggests that CCL19 and CXCL13 have distinct diffusion rates, and that CXCL13 exhibits both specific binding and diffusion at 6.6 ± 0.4 $\mu m^2 s^{-1}$ within the B-cell follicle.

Results

Overview of the high-speed single-molecule tracking methodology

To enable precise localization and tracking of rapidly diffusing biomolecules we modified the optical path of a standard inverted epifluorescence microscope (Fig. 1(a)) to implement a broadband laser whose output was selectable over wavelengths ~400-2,000 nm (Supplementary Fig. 1), spanning the excitation spectra of visible light and near infrared fluorophores; the beam was de-expanded using a series of lenses to generate a narrow illumination field of ~12 µm full width at half maximum which could be switched from epifluorescence into total internal reflection fluorescence (TIRF) by controllable translation of a lens, although TIRF was not used in this work. High contrast epifluorescence images magnified to 120 nm/pixel were captured by an ultrasensitive back-illuminated EMCCD detector (860 iXon+, Andor Technology Ltd.) which could be sub-arrayed to 29x128 pixels to enable rapid frame rates of 1,515 Hz. Images were analyzed using bespoke software (Miller et al., 2015) written in MATLAB (Mathworks), which enabled automated 2D sub-millisecond tracking of single fluorescent dye molecules and determination of the microscopic diffusion coefficient D from the measured mean square displacement (Robson et al., 2013). Diffusion coefficients were found by an interative fitting procedure developed with simulated data.

Speed of tracking and image analysis

A range of sample exposure times of 0.44-1.98 ms per frame were used, with most data acquired at 0.59 ms per frame (0.65 ms cycle time) as a compromise between sampling speed and localization precision. In all cases we were able to resolve distinct diffusing fluorescent foci of measured 2D half width at half maximum in the range 250-300 nm, consistent with single point spread function (PSF) images. Automated foci tracking was utilized for the determination of molecular diffusivity. Foci could be tracked continuously in 2D with ~40 nm precision (Supplementary Fig. 4).

The presence of single molecules was determined by the observation of stepwise photobleaching steps. Examples of this are shown in Supplementary Fig. S1c,d,. From the manufacturers specifications BSA-AF647 was expected to be labeled with between 3-6 AF647 dye molecules and the chemokines were expected to be singly labeled. Only single molecule bleaching steps were observed in the chemokine data.

The initial intensity of observed foci of the AF647 dye molecule was measured in five conditions: CCL19-AF647 and CXCL13-AF647 in collagen and under heparan sulfate immobilization, and BSA-AF647 in 10% Ficoll. The kernel density estimate was found from the intercept of a line fitted to the first three intensity values measured. Within experimental error the initial intensity for all conditions fell in the 2000-3000 count range. The initial intensity is expected to vary for each condition due to the different local environment of the AF647 tag on each molecule, including different allowed orientations and varying flexibility of the linker. Further, the viscosity of the medium is known to affect the emission profile of AF647 and will cause slight variations in total measured intensity due to the use of a band pass filter in the emission path.

Analysis of the tracking data from CXCL13-AF647 and CCL19-AF647 using step-wise dye photobleaching showed predominantly monomeric populations for each (Fig. 2, Supplementary Fig. 1). Apparent stoichiometry values determined from the intensity of tracked fluorescent foci greater than one molecule per foci may be due to real multimeric complexes or potentially due to the overlap of monomeric foci images in the 2D projection that is imaged, especially in the case of high dye concentration. The maximum number of detected foci in one frame of 15 foci in our case was used in a random overlap model which assumes a Poisson distribution for nearest neighbor foci overlap probability (Llorente-Garcia et al., 2014; Wollman et al., 2017). This analysis indicates an 18% probability for random single foci overlap. The predicted intensity of foci due to random overlap could be obtained by convolving the intensity distribution of a single molecule of AF647 (width scaled by the square root of the apparent stoichiometry) with the apparent stoichiometry distribution generated by the random overlap probability prediction. The overlap model was found to be statistically identical to the experimentally observed distribution below apparent stoichiometry values of six AF647 molecules per foci ($p<0.05$, Pearson's χ^2 test). A small proportion of less than 5% of foci we found to have a higher apparent stoichiometry than that predicted from the random overlap model; it is possible that these may be indicative of some additional factors not captured in the basic overlap model such as non-uniformity in illumination across the field of view and experimental autofluorescence.

Iterative data simulation and experimental data fitting

Our analysis of the distribution of effective diffusion coefficients obtained from the single-molecule tracking data was corroborated through simulations of diffusing and immobilized foci using realistic signal and background noise values. Iterative cycles of simulation and experimental data fitting were used to determine initial parameters for fitting and the form of the fitting functions. All simulations were run and fitted with and without the addition of Gaussian white noise. The first simulated values were chosen by fitting the experimental data with a two gamma distribution model (Qian et al., 1991) to account for two diffusive populations.

Initially two distributions; 1.6 μm^2s^{-1} and a 50:50 mixed population of 1.6 μm^2s^{-1} and 10 μm^2s^{-1} were simulated (sample images in Fig. 3a). The data was plotted via kernel density estimation, and fitted with 1, 2 and 3 gamma distribution functions with 4 independent steps, all parameters constrained to be positive, each term was multiplied by a fractional prefactor to preserve the unity area of the kernel density plot, and the

χ^2 goodness-of-fit parameter was evaluated (Supplementary Table 1). The χ^2 statistic accounts for the number of free parameters in the fit, and is used to determine if decreasing residuals are caused by increasing the number of free parameters. For the one component distribution the one gamma fit gave the lowest χ^2, and for the two component distribution, the two gamma fit gave the lowest χ^2 value, as expected. Applying these three models to the experimental collagen and heparan sulfate immobilized chemokine data gave the lowest χ^2 for a two component fit, except for CCL19 in heparan sulfate, which contained a very low proportion of mobile tracks and was well fitted by a single component distribution. From this, it was determined that a two component distribution should be fitted to the experimental data.

The number of independent steps is usually taken to be the same as the number of steps analyzed in gamma distribution fitting analysis of microscopic diffusion coefficients, where it is a parameter governing the shape of the distribution. Strictly, steps are only independent when non-overlapping steps are used (Qian et al., 1991), but when the localization precision (in nm) of single particles is small compared to the distance moved between localizations in a track the diffusion coefficient distributions from overlapping steps are still well-approximated by the assumption of independent steps. In this work, the temporal resolution is increased to a level where the localization precision is no longer negligible compared to the distance moved between localizations, and steps containing the same localizations are no longer well approximated as being independent. To investigate the independence of the steps in the data and determine the relevant fitting parameter, simulations of 1.6 $\mu m^2 s^{-1}$ and 10 $\mu m^2 s^{-1}$ were made separately, and fitted with a single component gamma distribution where the number of independent steps was allowed to vary. The results (Table 1) indicate this value to be around two, in line with expectations of consecutive steps containing the same localization not being independent, reducing the number of steps by half.

Fitting simulations of a 50:50 population of molecules with diffusion coefficients of 1.6 $\mu m^2 s^{-1}$ and 10 $\mu m^2 s^{-1}$ with two gamma distributions with the same fitted value of N in each distribution, and N constrained to be in the range 0-4, (Fig. 3b and Supplementary Table 2), gives a distribution which does not match the experimental data (Fig. 4a, 5d-e): when the data is placed in a histogram based on measured diffusion coefficient the experimental data shows a peak in the first bin width, which is not seen in the simulation of 1.6 $\mu m^2 s^{-1}$ data. The 1.6 $\mu m^2 s^{-1}$ data was simulated because this was found as a preliminary result of fitting to the experimental data, but a simulation of truly immobile data with a diffusion coefficient of 0 $\mu m^2 s^{-1}$ gave a peak in the first bin of the histogram when put into bins with the width of the localization precision (see Fig. 3c), matching the experimental data.

Our simulated particle diffusion analysis suggests that the low mobility population in the experimental data is immobile at the level of the localization precision. Fitting the distribution of simulated 0 $\mu m^2 s^{-1}$ data with a single gamma distribution gave a value of N less than one, and requires the fit applied to the experimental data to include a different value of N in the distribution fitted to each population; with the value of N being less than one for the low mobility population, and two for the higher mobility population.

Applying this fit, with the constraint that the diffusion coefficient of the immobile population must fall within the first bin of the histogram, gave the fitted experimental diffusion coefficients. To qualitatively compare the simulated and experimental data, a mixed simulation of 0 and 9 $\mu m^2 s^{-1}$ data with Gaussian white noise was performed and fitted in the same way, giving a diffusion coefficient for the mobile peak of 8.9 ± 0.4 $\mu m^2 s^{-1}$. The distribution is similar in profile to the data for CCL19-AF647 in collagen (see Fig. 3d).

Diffusion in buffer and Ficoll solutions

In PBS buffer alone the chemokine diffusion was in general too fast to track over consecutive image frames (Supplementary Video 1). Whilst this is consistent with theoretical estimates using the Stokes-Einstein relation which gives D ~150 $\mu m^2/s$ for chemokines in an aqueous environment, the application of 10% Ficoll increased the fluid viscosity by a factor of 5.6 to 0.005 Pa.s, which enabled single particle tracking; if diffusion had been well modelled by the Stokes-Einstein relation the diffusion coefficients in the higher viscosity Ficoll solution would be expected to be ~30 $\mu m^2/s$ and particles would still not be tracked. The ability to track single chemokines in a medium of this viscosity demonstrates that the theory is not adequate to describe chemokine diffusion and motivates our experimental measurements.

The experimental system was tested first on a non-chemokine control of AF647-tagged BSA (BSA-AF647). The results of single particle tracking of BSA-AF647 were consistent with a proportion of immobile tracks associated with the coverslip surface and a freely diffusing mobile population with $D_{mobile} = 9.3 \pm 0.4$ $\mu m^2 s^{-1}$ (Fig. 4 and Supplementary Video 2,3). Including theoretical expectations based on hydrodynamic modeling of BSA as a Stokes sphere of radius 3.48 nm for monomeric BSA, with a monomer to dimer ratio of 15:2 (measured using SEC-MALLS quantification, Supplementary Fig. 2 Supplementary Table 3) and incorporating Faxen's law for distances of 10 nm, at which distances increased viscosity effects occur at the coverslip boundary (Axelsson, 1978), the fitted mobile value is found to be in agreement with the theoretical value of 9.4 $\mu m^2 s^{-1}$.

Comparison of SMT with FCS and FRAP

The diffusion coefficient of AF647 labeled BSA in a Ficoll solution was additionally measured with FCS and FRAP to generate a comparison of the three methods in a complex, non-surface environment (Supplementary Fig. 3a-e). FRAP and FCS gave diffusion coefficients of 7.1 ± 0.3 $\mu m^2 s^{-1}$ and 18.8 ± 0.3 $\mu m^2 s^{-1}$ respectively (Fig. 4b,c, Table 2). The values found for the diffusion coefficients by these methods are summarized in Table 1 with the number of traces used for each measurement. The result for FCS is higher than the theoretical value, whilst that for FRAP is significantly lower even considering Faxen's law, temperature fluctuation and non-monomer content in BSA measured by SEC-MALLS (Supplementary Fig. 2 and Supplementary Table 3), however the effects of using an axially thin sample and including only 2D recovery in the FRAP analysis were not accounted for.

The FRAP and FCS results differ by a factor of 2.6, in general agreement with previous results from others in which diffusion coefficients found by FCS are mostly higher than those found by FRAP (Guo et al., 2008), with FCS giving values up to an order of magnitude higher than the values found by FRAP (Adkins et al., 2007; Calizo and Scarlata, 2013) and often attributed to the different spatial scales of the two measurements or the high number of assumptions required in fitting FRAP data (Macháň et al., 2016), such as the profile of the bleaching laser, which are likely to be factors in the experiments performed here. The value found by SMT was the closest to the theoretical estimate of the diffusion coefficient in Ficoll of the experimental viscosity.

FCS and FRAP were also performed on the chemokines in 10% Ficoll 400. FCS produced autocorrelation curves with similar amplitude to BSA-AF647, but high variation was observed in the relative sizes and characteristic decay times of the triplet and translational diffusion populations (Supplementary figure 3f), resulting in no consensus value of the diffusion coefficient. Both FCS and FRAP measurements were hindered by the presence of large multimers of chemokine (Supplementary Fig. 3g). Multimers of this type are simply avoided by visual identification in single molecule tracking experiments.

Diffusion coefficients of CXCL13 and CCL19 in collagen

The values of the diffusion coefficients were determined in collagen reconstituted from rat tails to produce a simplified tissue mimic. The structure of the collagen was checked for the required formation of non-centrosymmetric structure with second-harmonic imaging microscopy (SHIM) (see Fig. 5a,b). The fibril diameters observed are in agreement with those seen by Chen *et al.* (Chen et al., 2012), and show qualitatively similar structure.

The values of the diffusion coefficients of CXCL13 and CCL19 in collagen were found by fitting a two gamma distribution to a histogram of the single-molecule tracking data with bin width of 40 nm given by peaks in the localization precision at low diffusion coefficient found from heparan sulfate immobilization of the labelled chemokines (Supplementary Fig. 4a,b, Supplementary videos 7,8). Heparan sulfate immobilization was verified by an extremely high proportion of immobile tracks (Supplementary Fig. 4c,d). The results of the fitting are given in Table 3, and the distributions for each chemokine showing the mobile and immobile populations are shown in Fig. 5c-e with sample images shown in Fig. 5c. The relative size of the mobile and immobile populations cannot be accurately accounted for as immobile populations were photobleached to enable imaging of highly diffuse mobile populations.

Modeling the sub-millisecond tracking data as a mixture of immobilized and mobile tracks generated excellent agreement to the experimental data (Table 3). Our findings indicated a higher diffusion coefficient for CCL19-AF647 than for CXCL13-AF647 in the controlled environment of collagen (Fig. 5f and Supplementary Videos 4,5), which we measured as 8.4 ± 0.2 $\mu m^2 s^{-1}$ and 6.2 ± 0.3 $\mu m^2 s^{-1}$ respectively. This heterogeneity is consistent with molecular mass expectations and may contribute to the formation of distinct spatial patterning profiles *in situ.*

Binding of CXCL13 to lymph node tissue sections

The experiments with BSA-AF647, CCL19-AF647 and CXCL13-AF647 in collagen suggested a 4-6 times higher proportion of molecules in the immobile fraction than the mobile fraction for the chemokines than for BSA-AF647, even allowing for differences introduced by utilizing a pre-bleach to increase the fraction of mobile tracks. This is in agreement with previous results: CXCL13 is secreted in soluble form, but is known to interact with extracellular matrix components (Monneau et al., 2017) and thus is likely to comprise a significant immobile fraction. To assess both fractions while also ensuring a sufficiently low concentration of CXCL13-AF647 to enable single molecule detection, we incubated murine lymph node tissue cryosections with CXCL13-AF647 and performed a short wash step. Whilst removing a large component of the soluble fraction of CXCL13-AF647, this preparation facilitated tracking of both mobile and immobile fractions of CXCL13-AF647 *in situ,* depending on the microscopy method employed.

To assess the specificity of binding we used confocal microscopy to quantify the fluorescent intensity of B220$^+$ regions (Fig. 6a) of lymph node tissue sections that had been incubated with either CXCL13-AF647 or BSA-AF647. The fluorescent intensity values obtained were significantly higher for samples incubated with CXCL13-AF647 (Fig. 6b,c), suggesting that the binding of CXCL13 to lymph node follicles was specific.

In the single molecule microscopy experiments we imaged and tracked CXCL13-AF647 in B cell follicles of *ex vivo* murine lymph node tissue sections with super-resolution precision at ~2 ms timescales (Fig. 7c and Supplementary Video 6), determining the precise location in the tissue using FITCB220 (B cell specific marker) (Supplementary Fig. 5). Auto-fluorescent extracellular matrix (ECM) components were localized by the tracking software and were segmented to allow discrimination of tracks from the immobile ECM and the diffusing chemokine (Fig. 7c,d,f). When the same segmentation analysis was performed on control tissue sections prepared by the same protocol except without the addition of CXCL13-AF647, similar autofluorescent structures were seen and could be segmented (see Fig. 7a,b). The observed diffusion coefficient distribution of tracked extracellular matrix regions within the B-cell follicle in the presence of chemokine were observed to be skewed towards higher mobility than those in the absence of chemokine (Fig. 7e), further confirming the presence of specific binding of CXCL13-AF647 in the extracellular matrix regions.

Diffusion coefficient of CXCL13 in lymph node tissue sections

For the same single-molecule imaging experiments performed at at ~2 ms timescales described above, after discrimination of mobile and immobile tracks by segmentation, the diffusion coefficient of mobile tracked particles for the field of view shown was fitted with a single gamma distribution indicating $D = 6.6 \pm 0.4\ \mu m^2 s^{-1}$ (Fig. 7g). Due to the inclusion of a wash step in our sample preparation we expect the majority of the mobile particles to be in the interstitial spaces between cells, although a small fraction may be within cut cells due to the preparation of tissue sections. The lack of fluorescent localizations in the central gap in the control sample is further evidence that the mobile population observed in the data is CXCL13-AF647.

To validate our result we performed a simulation of the conditions in the tissue, with the mean background level and standard deviation of the noise taken from the control data. 1000 frames of data of particles with diffusion coefficient 6.6 $\mu m^2 s^{-1}$ were generated, with spot intensities and spot widths taken from the experimental data for tracking in tissue. Sample images from the simulation can be seen in supplementary figure 6(a). The result of fitting this simulation was $D = 7.0 \pm 0.4$ $\mu m^2 s^{-1}$ (supplementary figure 6(b)), in agreement with the simulated value. Taken together, this demonstrates the ability of our method to extract diffusion coefficients from challenging experimental data.

Discussion

In this work, we have demonstrated the application of a high-speed single-molecule tracking microscopy system that is compatible with traditional widefield light microscopes. We compared our method with the traditional methods to measure molecular mobility of FCS and FRAP using one of the standard test molecules for molecular mobility (BSA). We applied this new approach to investigating hitherto unquantified molecular mobility of chemokines in complex environments, finding values of diffusion coefficients of 8.4 ± 0.2 $\mu m^2 s^{-1}$ for CCL19-AF647 and 6.2 ± 0.3 $\mu m^2 s^{-1}$ for CXCL13-AF647 in collagen, and of 6.6 ± 0.4 $\mu m^2 s^{-1}$ for CXCL13-AF647 in lymph node follicles, in addition to identifying a specifically bound CXCL13-AF647 population in the B-cell follicle. While we demonstrate the efficacy of the approach on chemokines, this is a proof-of-concept for a more general scheme that could be applied to signaling lipids and cytokines.

Our method enables single-molecule tracking of organic dye probes at sub-millisecond timescales, down to less than half a millisecond per imaging frame whilst still enabling 40 nm localization precision in realistic tissue mimetic microenvironments. In *ex vivo* lymph node tissue sections, we were able to perform rapid super-resolution sampling down to 2ms per imaging frame and still achieve single-molecule detection sensitivity. To our knowledge this is the first application of sub-millisecond tracking of small fluorophores away from the coverslip interface.

We characterized the output of our single-molecule tracking tools with a range of simulations of mixed molecular mobility using realistic levels of signal and noise comparable to those exhibited at challenging single-molecule detection levels with very rapid sub-millisecond fluorescence sampling. We also tested our imaging and analysis methods using a fluorescently labeled version of the well-characterized molecule, BSA, and compared these with experiments using FRAP and FCS. The values of diffusion coefficient for mobile BSA determined using our rapid SMT method were in close agreement to expectations based on hydrodynamic modeling. Equivalent BSA mobility values estimated from using FRAP or FCS were less reliable. We compared the diffusion coefficients of BSA-AF647 measured by FCS, FRAP and SMT, producing a comparison of these techniques away from the coverslip interface, and showing agreement in the relation of the measured values with most previous studies performed on lipid bilayers, or on live cell plasma membranes.

We measured the diffusion coefficients of CXCL13-AF647 and CCL19-AF647 in reconstituted collagen, finding values of 6.2 ± 0.3 $\mu m^2 s^{-1}$ and 8.4 ± 0.2 $\mu m^2 s^{-1}$ respectively. We further measured the diffusion coefficient of CXCL13-AF647 in ex vivo lymph node tissue section, finding a value in agreement with that measured in collagen of 6.6 ± 0.4 $\mu m^2 s^{-1}$. Fluorescent tags increase the mass of the labelled molecule and potentially affect the properties of diffusion. The fluorophore used in this work, AF647, was chosen for its small mass, which is especially important here given the small mass of chemokines. This choice resulted in a ~10% increase in mass of the labelled chemokine compared to the unlabeled chemokine, but this is lower than would have been achieved with other fluorophores. Following the assumptions of the Stokes-Einstein model of a spherical protein of uniform density, a 10% increase in mass would only decrease the observed diffusion coefficient by ~3.2%. We observe a large discrepancy between our empirical measurements for chemokine diffusion rates and the higher estimated values derived on the basis of Stokes-Einstein relation. However, this discrepancy is of the same order of magnitude as that previously observed for the same theoretical calculation for GFP (~93 $\mu m^2 s^{-1}$) and measured experimental values in Escherichia Coli (~7.7-9 $\mu m^2 s^{-1}$ (Elowitz et al., 1999; Mullineaux et al., 2006)).This discrepancy may be indicative of additional factors that affect molecular mobility in tissues but are not captured in the simplistic Stokes-Einstein relation. These factors might include, for example, dynamic physical and chemical processes which result in more constrained mobility such as transient biochemical interactions within the localized microenvironment, as have been observed previously in studies which suggest that CXCL13 binds to extracellular matrix components (Monneau et al., 2017).

Placed in an immunological context, our data shows that chemokine mobility is multimodal in complex environments. Using our novel imaging approach we were able to quantitatively identify a mobile and immobile fraction in collagen, and using a combination of confocal microscopy and single-molecule imaging we identified mobile and bound populations of CXCL13-AF647 in lymph node follicles. Thus, it is important to consider the contributions of both populations of CXCL13 upon cellular behaviors, rather than taking a view where it acts in either a soluble or an immobile way. The properties, and likely highly constrained nature of CXCL13 diffusion within the follicle may provide an insight into how B-cells can form such tightly compartmentalized microanatomical structures such as the follicle, or the germinal center light-zone.

Our novel high-speed microscopy and analysis outperforms traditional molecular mobility tools of fluorescence recovery after photobleaching (FRAP) and fluorescence correlation spectroscopy (FCS) in being able to capture diffusional heterogeneity relevant to real, complex biological systems exemplified by underlying mobile and immobile states. The high time resolution achieved with our system enables rapid diffusion to be quantified in heterogeneous aqueous environments typical of interstitial regions between cells in tissues, whilst still retaining super-resolution spatial precision and single-molecule detection sensitivity, enabling new insight into complex systems. A key advantage of our rapid single particle tracking method is its ability to determine the underlying heterogeneity in the mobility of the molecular population exemplified here by chemokines that diffuse in different environments. Whilst we demonstrate the efficacy of the approach on chemokines, this is a proof-of-concept for a more general scheme that could be applied to lipids and cytokines. Our system is compatible with traditional widefield light microscopes as opposed to requiring expensive and dedicated super-resolution setups; this accessibility bodes well for establishing a significant future impact investigating multiple biological systems.

Materials and Methods

Reagents

Human CXCL13 and CCL19 (Almac, CAF-12 and CAF-06 respectively) singly labeled with the far-red fluorescent tag AF647 (molecular mass 1250 Da were stored in water at 222 μg/ml. This fluorophore was chosen because of its small molecular mass, which reduces the impact of increased mass on molecular mobility, and due to its excitation at the long, lower energy wavelength range of the spectrum, which reduces sample damage. Collagen samples contained type I collagen extracted from rat tails (Barnes et al., 2016) diluted in PBS to 3.3 mg/ml and chemokine at 111 ng/ml; samples were set to pH7 with the addition of NaOH. BSA labeled with 3-6 AF647 purchased from Thermo Fisher Scientific Inc. Ficoll 400 (Sigma-Aldrich) was diluted in PBS at 0.1g/ml to create a 10% solution of viscosity 0.005 Pa.s at room temperature (Rashid et al., 2015).

Preparation of collagen matrix in tunnel slides

Samples for fluorescence microscopy were prepared in tunnel slides formed by placing two parallel lines of double-sided tape on a standard microscopy slide around 5 mm apart. A plasma-cleaned coverslip was placed on top and carefully tapped down (avoiding the imaging area) to create a water-tight tunnel.

For imaging in a collagen matrix tunnel slides were cooled to 4˚C before addition of collagen and fluorescently labeled chemokines, and then incubated at 15˚C for 30 min, followed by an additional 30 min incubation at 37˚C. The collagen matrix was visualized using second harmonic imaging (Chen et al., 2012; Cox et al., 2003).

Immobilized chemokine samples were prepared by incubating a plasma-cleaned coverslip in heparan sulfate (Simon Davis and Parish, 2013) (50 mg/ml) (Sigma-Aldrich) in PBS for 30 min. Coverslips were washed with PBS and air dried for 30 min before tunnel slide assembly then 10nM fluorescently labeled chemokine solution in PBS was introduced to the tunnel slide and incubated in a humidity chamber for 15 min at 20˚C. Excess unbound chemokine was removed with a PBS wash.

SHIM imaging

Second harmonic imaging microscopy (SHIM) was performed on a Zeiss LSM 780 MP with a Zeiss invert microscope. Excitation at 900 nm wavelength (Coherent Ultra Laser) through a plan-apochromat 63x/1.4 oil objective lens was incident on the sample. Up converted light was collected via a 485 nm short pass filter onto a non-descanned detector.

Preparation of Lymph Node Tissue Sections

6-8 week old wild type mice (C57BL/6) were housed in BSF at the University of York. All experiments conformed to the ethical principles and guidelines approved by the University of York Institutional and Animal Care Use Committee. Popliteal Lymph Nodes were removed and excess fat or connective tissue removed with forceps. Samples were transferred to optimal cutting temperature medium (OCT, Tissue-Tek, Sakura Finetek) and snap frozen on dry ice samples and sectioned using a cryostat. 10 µm thick sections were cut and collected onto poly-L-Lysine coated microscope slides. Sections were dried overnight in the dark then stored at -20˚C.

Before use, lymph node sections on poly-L-lysine slides were incubated at room temperature for 30 min. Sections were hydrated in PBS for 5 min then air dried. Wax ImmEdge pen (Vector Laboratories) was used to draw a hydrophobic circle around each section to retain liquid on the section during staining. Sections were incubated in a blocking buffer of PBS 5% goat serum (Sigma) at room temperature for 1 hour. To determine where B cell follicular structures were located in the tissue we used the marker B220, a protein expressed on the surface of all murine B lymphocytes. After blocking, sections were incubated with an FITC conjugated antibody (RA3-6B2, purchased from eBioscience) that binds specifically to B220 diluted 1:200 in blocking buffer for 1 hour at room temperature. . After blocking, sections were incubated with an FITC conjugated antibody (RA3-6B2, purchased from eBioscience) that binds specifically to B220 diluted 1:200 in blocking buffer for 1 hour at room temperature. Samples were washed with PBS for 3 x 5 min.

For confocal microscopy experiments where exogeneous CXCL13-AF647/BSA-AF647 was used to measure binding to tissue, slides were stained with anti-B220 as described above followed by an incubation with 500nM of each fluorescently labelled protein for 1 hour at room temperature. Samples were then washed 1x 5 mins in PBS. A drop of Prolong gold (Invitrogen) was added to each section, and then a No 1.5 glass coverslip (Fisher) mounted on top. The slides were incubated overnight at 4°C the next day slides were sealed using nail varnish and stored at 4°C. Immunofluorescent stained sections were imaged using the Zeiss LSM 880 confocal microscope.

For single-molecule microscopy experiments sections were stained for B220 as described above, and then 1 μM of CXCL13-AF647 was added to the slides. Slides were incubated overnight at 4˚C after which slides were washed for 30 s in PBS and a coverslip (thickness 0.13-0.17mm, Menzel Gläser) mounted on top. Slides were then sealed and imaged.

Stokes model of diffusion

For a small sphere the diffusion coefficient is given by:

$$D = \frac{k_B T}{6\pi\eta r}$$

where k_B is the Boltzmann constant, T is room temperature, η is the dynamic viscosity of the media and r is the radius of a sphere, calculated assuming that the molecule is a globular protein of density 1.35 g.cm^{-3} (Fischer et al., 2004). The theoretical value of the diffusion coefficient of BSA in 10% Ficoll 400 was calculated using the Stokes radius of BSA of 3.48nm (Ikeda and Nishinari, 2000). The Stokes radius of a dimer was assumed be double the Stokes radius of a monomer.

Faxen's Law

At distances probed by narrowfield fluorescence microscopy (~ few hundred nanometres of the coverslip), the boundary effect of increased viscosity in the solution can be modeled by Faxen’s law (Happel and Brenner, 1981):

$$\eta(h) = \eta(\infty)\left(1 + P\left(\frac{r}{h}\right)\right)^{-1}$$

where $\eta(\infty) =$ dynamic laminar-flow viscosity in free solution, r is the radius of the particle, and h is the distance between the boundary and the center of the particle. To a 5th-order approximation:

$$P(\gamma) \approx -\frac{9\gamma}{16} + \left(\frac{\gamma}{8}\right)^3 - \left(\frac{45\gamma}{256}\right)^4 + \left(\frac{\gamma}{16}\right)^5$$

SEC-MALLS of BSA-AF647

The experimental system for SEC-MALLS experiments comprised a Wyatt HELEOS-II multi-angle light scattering detector and a Wyatt rEX refractive index detector attached to a Shimadzu HPLC system (SPD-20A UV detector, LC20-AD isocratic pump system, DGU-20A3 degasser and SIL-20A autosampler). 100 µl of 2.5 mg/ml BSA-AF647 sample was run at 0.5 ml/min flow rate at room temperature through superdex S200 columns (G.E. Healthcare) for 60 min in PBS running buffer. Peaks were integrated using Astra V software and the Zimm fit method with degree 1; a value of 0.183 was used for protein refractive index increment (dn/dc).

FCS and FRAP microscopy

FCS and FRAP experiments were performed on a Zeiss LSM 880 microscope, using a GaAsP detector. Samples were prepared in MatTek glass bottom petri dishes (1.5 coverglass, MatTek Corporation) and illuminated with a 633 nm wavelength laser.

For FCS the confocal volume was measured using a calibration sample of BSA-AF647 diffusion in water and constraining the diffusion coefficient to be 59 $\mu m^2 s^{-1}$ (Putnam, 1975); this allowed the structural parameter, s, to be fixed at 6.6. Three repeats of ten experiments were conducted, traces indicating the presence of multimeric clumps or proximity to the surface were excluded. Autocorrelation traces, $G(\tau)$, to account for transient dark states and translational diffusion were fitted with the equation:

$$G(\tau) = 1 + \left(1 + \frac{Te^{-\left(\frac{\tau}{\tau_T}\right)}}{1 - T}\right)\left(\frac{1}{V_{eff}\langle C\rangle}\frac{1}{\left(1 + \frac{\tau}{\tau_D}\right)}\frac{1}{\sqrt{1 + \left(\frac{1}{s}\right)^2 \frac{\tau}{\tau_D}}}\right)$$

where T is the triplet fraction, τ_T is the time constant of the dark state, τ_D is the time constant of translation across the confocal volume, V_{eff}, and $<C>$ is the average concentration. The diffusion coefficient, D, was calculated from τ_D via the equation:

$$D_{FCS} = \frac{{r_0}^2}{4\tau_D}$$

where r_0 is the spot width (0.322 µm). For FRAP microscopy a square region defined in the Zeiss Zen software was bleached with the 633 nm wavelength focused laser in an axially thin sample that was treated as being 2D. When applied to immobilized fluorophore the shape of the bleached area (see Fig. 4b) was found to be well approximated as a Gaussian spot of half-width ω = 4.9 ± 0.1 µm. To measure the diffusion coefficient of BSA-AF647 thirty recovery traces (intensity (I) vs time (t)) were acquired and fitted in the Zeiss Zen software with the single exponential equation:

$$I = I_0 - I_1 e^{\left(-\frac{t}{\tau_1}\right)}$$

where the initial intensity, I_0, drop in intensity, I_1, and the decay constant τ_1, from which the diffusion coefficient, D, is calculated via:

$$D_{FRAP} = \frac{\omega^2}{8\tau_1}$$

Single molecule fluorescence microscopy

Bespoke fluorescence microscopy was performed on an inverted microscope body (Nikon Eclipse Ti-S) with a 100x NA 1.49 Nikon oil immersion lens and illumination from a supercontinuum laser (Fianium SC-400-6, Fianium Ltd.), controlled with an acousto-optical tunable filter (AOTF) to produce excitation light centered on wavelength 619 nm (Supplementary Fig. 1). A 633 nm dichroic mirror and 647 nm long-pass emission filter were used beneath the objective lens turret to exclude illumination light from the fluorescence images. The sample was illuminated with narrowfield excitation of 12 µm FWHM and an intensity of 2,300 $W.cm^{-2}$. Images were recorded on an EMCCD camera (860 iXon+, Andor Technology Ltd) cooled to -80°C. 128x128 pixel images were acquired with 1.98 ms exposure times and 128 x 29 pixel image strips were acquired with 0.59 ms exposure times, both for 1,000 frames at the full EM and pre-amplifier gains of 300 and 4.6 respectively.

Particle Tracking and calculation of diffusion coefficients

All image data were recorded into .tiff files and analyzed in bespoke Matlab software. Single fluorescent molecules were identified and processed into super-resolution tracks using ADEMS code (Miller et al., 2015). The microscopic diffusion coefficient was calculated for each tracked particle from the gradient of a linear relation fitted to a plot of the mean square displacements against the four different step time intervals that can be calculated from the first four steps in a track. The microscopic diffusion coefficient distributions comprised an immobile fraction that had non-specifically adhered to the plasma-cleaned coverslip and a diffusive fraction. Microscopic diffusion coefficients were binned into histograms with bin width given by the localization precision of the immobilized (heparan sulfate) data. The probability distribution of diffusion coefficients was modeled by a gamma distribution (Qian et al., 1991; Saxton, 1997; Vrljic et al., 2002; Zawadzki et al., 2015):

$$F(x, D, N) = \frac{\left(\frac{N}{D}\right)^N x^{N-1} e^{-\frac{Nx}{D}}}{(N-1)!}$$

where N is the number of independent steps in a track and D is the true diffusion coefficient. The histogram data was fitted iteratively with a two-gamma distribution to account for the mobile and immobile fractions. Initial fitting constraints conserved the number of tracks and assumed the number of independent steps in a track was 4 or less, giving a first estimation of the diffusion coefficients. Then fluorescence microscopy data with the found diffusion coefficients was simulated with and without noise, tracked, and the distribution of diffusion coefficients was fitted with the same constraints as the actual data. Fitting parameters were refined based on the results of fitting to the simulated data, and the experimental data was fitted with the refined constraints. The process of simulating the data, fitting the simulation to refine the constraints and fitting the experimental data was repeated until the simulation represented the experimental data and the fit to the simulation data converged to the diffusion coefficient values simulated.

For immobilized spots the N value was less than 1, implying that the steps are not independent. This is expected for immobile molecules as the localization precision uncertainty is larger than the diffusion distance. For mobile spots N was fixed at two as there are two steps that do not contain any common localizations when only the first four steps of a track are used.

Simulation of fluorescence microscopy data.

Image datasets were simulated in bespoke MATLAB software at given diffusion coefficients using foci intensity, foci spot width, background intensity and foci density data from real images. Foci are created at random locations in the image frame with intensity randomly chosen from a localization in an experimental dataset. The new positions of a focus in the x and y directions after initial generation are each determined from a Gaussian distribution centered on the previous spot location with a standard deviation of the mean square displacement of a particle in one direction, $2Dt$, where D is the simulated diffusion coefficient and t is the time interval between frames. To incorporate photobleaching and other effects causing truncation of trajectories foci were randomly reassigned to a new location 10% of the time, however diffusion within a frame was not explicitly incorporated into the model beyond the use of the spot width of real localisations. The resulting image stack was used for no-noise simulations. Readout noise in the detector was incorporated in the simulations by the addition of zero mean Gaussian white noise, the intensity of which depended on the local intensity. For tissue data simulation the mean background level and standard deviation of the noise were taken from control data, away from autofluorescent ECM.

Bootstrapping

Errors on the found values of the diffusion coefficients from FRAP, FCS and single molecule tracking were found by bootstrapping (Asbury et al., 2003; Efron and Tibshirani, 1994). In this method, a randomly chosen 80% of the data is fitted in the same way as the entire data set and the standard deviation on each parameter from ten repeats of this process is taken as the error on each fit parameter found from 100% of the data.

Single molecule imaging in tissue sections

Tissue sections were stained with a FITC-conjugated antibody that binds B220 (RA3-6B2, purchased from eBioscience). Tissue sections were subsequently imaged at low (1.2 µm/pixel) magnification with green illumination (wavelength 470 nm (Supplementary Fig. 1), 12 µm FWHM, intensity of 875 W.cm^{-2}) to determine the location of the B cell follicles, before switching to high (120 nm/pixel) magnification and red illumination to image chemokines in these areas.

Segmentation of tissue sections images

Image acquisitions in tissue contain regions of autofluorescent ECM (see Supplementary Note and Supplementary Fig. 5) which are identified by the tracking software. These images must be segmented to identify tracks due to fluorescently labeled chemokine or ECM. Intensity averages of the image acquisition were top hat filtered with a structuring element of radius 4 pixels. The resulting image was converted to binary form using a threshold defined by Otsu's method and the binary image used to enhance the extracellular matrix regions of the original image. Small holes in the thresholded region were filled by sequential erosion and dilation with a disk of radius 2 pixels as the structuring element.

Code availability

All our bespoke software developed is freely and openly accessible via https://sourceforge.net/projects/york-biophysics/

Statistics

Goodness-of-fit values for modeling of the distribution of microscopic diffusion coefficients were evaluated using χ^2 tests as detailed in the text. Experimentally measured stoichiometry distributions were compared against random overlap predictions in a pairwise fashion where appropriate using Pearson's χ^2 test.

Acknowledgments

Supported by the Biological Physical Sciences Institute (BPSI), MRC grants MR/K01580X/1 (P.O.T. and M.C.L), MC_PC_15073 (M.C.C. and M.C.L) and BBSRC grant BB/N006453/1 (A.J.M.W. and M.C.L.). J.C. is supported by a studentship from the Wellcome Trust 4-year PhD programme (WT095024MA): Combating Infectious Disease: Computational Approaches in Translation Science. The authors thank Jo Marrison and Andrew Leech (Bioscience Technology Facility, University of York) for technical assistance with FCS and FRAP microscopy, and for SEC-MALLs respectively, Chris Power (Carl Zeiss Microscopy) for help with FCS, and Anne Theury for providing lymph node tissue sections.

Author Contributions

H.M. built the bespoke fluorescence microscope, overseen by M.C.L.; J.C. prepared biological samples overseen by M.C.C. H.M. and J.C. performed the imaging except the confocal microscopy showing binding specificity of CXCL13-AF647 performed and analyzed by E.T. and Z.Z. A.W. performed the overlap calculations. H.M. analyzed all other data with input from A.W., M.C.L.. H.M. ran simulations of fluorescence data on code adapted from A.W.. P.O.T. oversaw FCS and FRAP microscopy. H.M., A.W., E.T. prepared the figures with input from all authors. H.M., J.C., and M.C.L. wrote the manuscript with input from all authors.

Competing financial interests

The authors declare no competing financial interests.

References

Adkins, E. M., Samuvel, D. J., Fog, J. U., Eriksen, J., Jayanthi, L. D., Vaegter, C. B., et al. (2007). Membrane Mobility and Microdomain Association of the Dopamine Transporter Studied with Fluorescence Correlation Spectroscopy and Fluorescence Recovery after Photobleaching. *Biochemistry* 46, 10484–97. doi:10.1021/BI700429Z.

Andrecka, J., Ortega Arroyo, J., Takagi, Y., de Wit, G., Fineberg, A., MacKinnon, L., et al. (2015). Structural dynamics of myosin 5 during processive motion revealed by interferometric scattering microscopy. *Elife* 4, 393–414. doi:10.7554/eLife.05413.

Asbury, C. L., Fehr, A. N., and Block, S. M. (2003). Kinesin Moves by an Asymmetric Hand-Over-Hand Mechanism. *Science (80-.).* 302.

Ashley, T. T., Gan, E. L., Pan, J., and Andersson, S. B. (2016). Tracking single fluorescent particles in three dimensions via extremum seeking. *Biomed. Opt. Express* 7, 3355–3376. doi:10.1364/BOE.7.003355.

Axelrod, D., Koppel, D. E., Schlessinger, J., Elson, E., and Webb, W. W. (1976a). Mobility measurement by analysis of fluorescence photobleaching recovery kinetics. *Biophys. J.* 16, 1055–1069. doi:10.1016/S0006-3495(76)85755-4.

Axelrod, D., Ravdin, P., Koppel, D. E., Schlessinger, J., Webb, W. W., Elson, E. L., et al. (1976b). Lateral motion of fluorescently labeled acetylcholine receptors in membranes of developing muscle fibers. *Proc. Natl. Acad. Sci. U. S. A.* 73, 4594–8..

Axelsson, I. (1978). Characterization of proteins and other macromolecules by agarose gel chromatography. *J. Chromatogr. A* 152, 21–32. doi:10.1016/S0021-9673(00)85330-3.

Balzarotti, F., Eilers, Y., Gwosch, K. C., Gynnå, A. H., Westphal, V., Stefani, F. D., et al. (2017). Nanometer resolution imaging and tracking of fluorescent molecules with minimal photon fluxes. *Science (80-.).* 355, 606–612.

Barnes, A. L., Genever, P. G., Rimmer, S., and Coles, M. C. (2016). Collagen–Poly(N -isopropylacrylamide) Hydrogels with Tunable Properties. *Biomacromolecules* 17, 723–734. doi:10.1021/acs.biomac.5b01251.

Bennett, L. D., Fox, J. M., and Signoret, N. (2011). Mechanisms regulating chemokine receptor activity. *Immunology* 134, 246–256. doi:10.1111/j.1365-2567.2011.03485.x.

Betzig, E., Patterson, G. H., Sougrat, R., Lindwasser, O. W., Olenych, S., Bonifacino, J. S., et al. (2006). Imaging intracellular fluorescent proteins at nanometer resolution. *Science* 313, 1642–5. doi:10.1126/science.1127344.

Buckley, C. D., Barone, F., Nayar, S., Bénézech, C., and Caamaño, J. (2015). Stromal Cells in Chronic Inflammation and Tertiary Lymphoid Organ Formation. *Annu. Rev. Immunol.* 33, 715–745. doi:10.1146/annurev-immunol-032713-120252.

Calizo, R. C., and Scarlata, S. (2013). Discrepancy between fluorescence correlation spectroscopy and fluorescence recovery after photobleaching diffusion measurements of G-protein-coupled receptors. *Anal. Biochem.* 440, 40–48. doi:10.1016/j.ab.2013.04.033.

Chen, X., Nadiarynkh, O., Plotnikov, S., and Campagnola, P. J. (2012). Second harmonic generation microscopy for quantitative analysis of collagen fibrillar structure. *Nat. Protoc.* 7, 654–669. doi:10.1038/nprot.2012.009.

Colditz, I. G., Schneider, M. A., Pruenster, M., and Rot, A. (2007). Chemokines at large: in-vivo mechanisms of their transport, presentation and clearance. *Thromb. Haemost.* 97, 688–693.

Cox, G., Kable, E., Jones, A., Fraser, I., Manconi, F., and Gorrell, M. D. (2003). 3-Dimensional imaging of collagen using second harmonic generation. *J. Struct. Biol.* 141, 53–62. doi:10.1016/S1047-8477(02)00576-2.

Drayton, D. L., Liao, S., Mounzer, R. H., and Ruddle, N. H. (2006). Lymphoid organ development: from ontogeny to neogenesis. *Nat. Immunol.* 7, 344–353. doi:10.1038/ni1330.

Dustin, M. L., and Baldari, C. T. (2017). “The Immune Synapse: Past, Present, and Future,” in *Methods in molecular biology (Clifton, N.J.)*, 1–5. doi:10.1007/978-1-4939-6881-7_1.

Edidin, M., Zagyansky, Y., and Lardner, T. (1976). Measurement of membrane protein lateral diffusion in single cells. *Science (80-.).* 191, 466–468.

Efron, B., and Tibshirani, R. (1994). *An introduction to the bootstrap*. Chapman & Hall

Ehrenberg, M., and Rigler, R. (1974). Rotational brownian motion and fluorescence intensify fluctuations. *Chem. Phys.* 4, 390–401. doi:10.1016/0301-0104(74)85005-6.

Einstein, A. (1905). Über die von der molekularkinetischen Theorie der Wärme geforderte Bewegung von in ruhenden Flüssigkeiten suspendierten Teilchen. *Ann. Phys.* 322, 549–560. doi:10.1002/andp.19053220806.

Elowitz, M. B., Surette, M. G., Wolf, P. E., Stock, J. B., and Leibler, S. (1999). Protein mobility in the cytoplasm of Escherichia coli. *J. Bacteriol.* 181, 197–203.

Fischer, H., Polikarpov, I., and Craievich, A. F. (2004). Average protein density is a molecular-weight-dependent function. *Protein Sci.* 13, 2825–8. doi:10.1110/ps.04688204.

Fujiwara, T., Ritchie, K., Murakoshi, H., Jacobson, K., and Kusumi, A. (2002). Phospholipids undergo hop diffusion in compartmentalized cell membrane. *J. Cell Biol.* 157, 1071–81. doi:10.1083/jcb.200202050.

Guo, L., Har, J. Y., Sankaran, J., Hong, Y., Kannan, B., and Wohland, T. (2008). Molecular Diffusion Measurement in Lipid Bilayers over Wide Concentration Ranges: A Comparative Study. *ChemPhysChem* 9, 721–728. doi:10.1002/cphc.200700611.

Gustafsson, M. G. (2000). Surpassing the lateral resolution limit by a factor of two using structured illumination microscopy. *J. Microsc.* 198, 82–7.

Happel, J., and Brenner, H. (1981). *Low Reynolds number hydrodynamics : with special applications to particulate media*. Springer Netherlands

Hell, S. W., and Wichmann, J. (1994). Breaking the diffraction resolution limit by stimulated emission: stimulated-emission-depletion fluorescence microscopy. *Opt. Lett.* 19, 780–2.

Hiramoto-Yamaki, N., Tanaka, K. A. K., Suzuki, K. G. N., Hirosawa, K. M., Miyahara, M. S. H., Kalay, Z., et al. (2014). Ultrafast Diffusion of a Fluorescent Cholesterol Analog in Compartmentalized Plasma Membranes. *Traffic* 15, 583–612. doi:10.1111/tra.12163.

Ikeda, S., and Nishinari, K. (2000). Intermolecular Forces in Bovine Serum Albumin Solutions Exhibiting Solidlike Mechanical Behaviors. *Biomacromolecules* 1, 757–763. doi:10.1021/BM005587O.

Juette, M. F., and Bewersdorf, J. (2010). Three-Dimensional Tracking of Single Fluorescent Particles with Submillisecond Temporal Resolution. *Nano Lett.* 10, 4657–4663. doi:10.1021/nl1028792.

Kienle, K., and Lämmermann, T. (2016). Neutrophil swarming: an essential process of the neutrophil tissue response. *Immunol. Rev.* 273, 76–93. doi:10.1111/imr.12458.

Lagerholm, B. C., Andrade, D. M., Clausen, M. P., and Eggeling, C. (2017). Convergence of lateral dynamic measurements in the plasma membrane of live cells from single particle tracking and STED-FCS. *J. Phys. D. Appl. Phys.* 50, 63001.

Leake, M. C. (2013). The physics of life: one molecule at a time. *Philos. Trans. R. Soc. Lond. B. Biol. Sci.* 368, 20120248. doi:10.1098/rstb.2012.0248.

Llorente-Garcia, I., Lenn, T., Erhardt, H., Harriman, O. L., Liu, L.-N., Robson, A., et al. (2014). Single-molecule in vivo imaging of bacterial respiratory complexes indicates delocalized oxidative phosphorylation. *Biochim. Biophys. Acta* 1837, 811–24. doi:10.1016/j.bbabio.2014.01.020.

Macháň, R., Foo, Y. H., and Wohland, T. (2016). On the Equivalence of FCS and FRAP: Simultaneous Lipid Membrane Measurements. *Biophys. J.* 111, 152–161. doi:10.1016/j.bpj.2016.06.001.

Magde, D., Elson, E., and Webb, W. W. (1972). Thermodynamic Fluctuations in a Reacting System—Measurement by Fluorescence Correlation Spectroscopy. *Phys. Rev. Lett.* 29, 705–708. doi:10.1103/PhysRevLett.29.705.

Miller, H., Zhou, Z., Shepherd, J., Wollman, A. J. M., and Leake, M. C. (2018). Single-molecule techniques in biophysics: a review of the progress in methods and applications. *Reports Prog. Phys.* 81, 24601. doi:10.1088/1361-6633/aa8a02.

Miller, H., Zhou, Z., Wollman, A. J. M., and Leake, M. C. (2015). Superresolution imaging of single DNA molecules using stochastic photoblinking of minor groove and intercalating dyes. *Methods* 88, 81–88. doi:10.1016/j.ymeth.2015.01.010.

Monneau, Y. R., Luo, L., Sankaranarayanan, N. V., Nagarajan, B., Vivès, R. R., Baleux, F., et al. (2017). Solution structure of CXCL13 and heparan sulfate binding show that GAG binding site and cellular signalling rely on distinct domains. *Open Biol.* 7, 170133. doi:10.1098/rsob.170133.

Mullineaux, C. W., Nenninger, A., Ray, N., and Robinson, C. (2006). Diffusion of green fluorescent protein in three cell environments in Escherichia coli. *J. Bacteriol.* 188, 3442–8. doi:10.1128/JB.188.10.3442-3448.2006.

Pereira, J. P., Kelly, L. M., and Cyster, J. G. (2010). Finding the right niche: B-cell migration in the early phases of T-dependent antibody responses. *Int. Immunol.* 22, 413–9. doi:10.1093/intimm/dxq047.

Piliarik, M., and Sandoghdar, V. (2014). Direct optical sensing of single unlabelled proteins and super-resolution imaging of their binding sites. *Nat. Commun.* 5. doi:10.1038/ncomms5495.

Plank, M., Wadhams, G. H., and Leake, M. C. (2009). Millisecond timescale slimfield imaging and automated quantification of single fluorescent protein molecules for use in probing complex biological processes. *Integr. Biol.* 1, 602–12. doi:10.1039/b907837a.

Putnam, F. (1975). *The Plasma Proteins : Structure, Function, and Genetic Control.*

Second. Academic Press, New York.

Qian, H., Sheetz, M. P., and Elson, E. L. (1991). Single particle tracking. Analysis of diffusion and flow in two-dimensional systems. *Biophys. J.* 60, 910–21. doi:10.1016/S0006-3495(91)82125-7.

Rashid, R., Chee, S. M. L., Raghunath, M., and Wohland, T. (2015). Macromolecular crowding gives rise to microviscosity, anomalous diffusion and accelerated actin polymerization. *Phys. Biol.* 12, 34001. doi:10.1088/1478-3975/12/3/034001.

Reyes-Lamothe, R., Sherratt, D. J., and Leake, M. C. (2010). Stoichiometry and architecture of active DNA replication machinery in Escherichia coli. *Science* 328, 498–501. doi:10.1126/science.1185757.

Robson, A., Burrage, K., and Leake, M. C. (2013). Inferring diffusion in single live cells at the single-molecule level. *Philos. Trans. R. Soc. Lond. B. Biol. Sci.* 368, 20120029. doi:10.1098/rstb.2012.0029.

Rot, A., and von Andrian, U. H. (2004). Chemokines in innate and adaptive host defense: basic chemokinese grammar for immune cells. *Annu. Rev. Immunol.* 22, 891–928. doi:10.1146/annurev.immunol.22.012703.104543.

Rust, M. J., Bates, M., and Zhuang, X. (2006). Sub-diffraction-limit imaging by stochastic optical reconstruction microscopy (STORM). *Nature* 3, 793–795. doi:10.1038/NMETH929.

Saxton, M. J. (1997). Single-particle tracking: the distribution of diffusion coefficients. *Biophys. J.* 72, 1744–1753. doi:10.1016/S0006-3495(97)78820-9.

Schneider, J., Zahn, J., Maglione, M., Sigrist, S. J., Marquard, J., Chojnacki, J., et al. (2015). Ultrafast, temporally stochastic STED nanoscopy of millisecond dynamics. *Nat. Methods* 12, 827–30. doi:10.1038/nmeth.3481.

Schulz, O., Hammerschmidt, S. I., Moschovakis, G. L., and Förster, R. (2016). Chemokines and Chemokine Receptors in Lymphoid Tissue Dynamics. *Annu. Rev. Immunol.* 34, 203–242. doi:10.1146/annurev-immunol-041015-055649.

Simon Davis, D. A., and Parish, C. R. (2013). Heparan sulfate: a ubiquitous glycosaminoglycan with multiple roles in immunity. *Front. Immunol.* 4, 470. doi:10.3389/fimmu.2013.00470.

Song, L., Lu-Walther, H.-W., Förster, R., Jost, A., Kielhorn, M., Zhou, J., et al. (2016). Fast structured illumination microscopy using rolling shutter cameras. *Meas. Sci. Technol.* 27, 55401. doi:10.1088/0957-0233/27/5/055401.

van 't Hoff, M., de Sars, V., and Oheim, M. (2008). A programmable light engine for quantitative single molecule TIRF and HILO imaging. *Opt. Express* 16, 18495. doi:10.1364/OE.16.018495.

von Hundelshausen, P., Agten, S. M., Eckardt, V., Blanchet, X., Schmitt, M. M., Ippel, H., et al. (2017). Chemokine interactome mapping enables tailored intervention in acute and chronic inflammation. *Sci. Transl. Med.* 9.

Vrljic, M., Nishimura, S. Y., Brasselet, S., Moerner, W. E., and McConnell, H. M. (2002). Translational diffusion of individual class II MHC membrane proteins in cells. *Biophys. J.* 83, 2681–92. doi:10.1016/S0006-3495(02)75277-6.

Wieser, S., Moertelmaier, M., Fuertbauer, E., Stockinger, H., and Schütz, G. J. (2007). (Un)confined diffusion of CD59 in the plasma membrane determined by high-resolution single molecule microscopy. *Biophys. J.* 92, 3719–28. doi:10.1529/biophysj.106.095398.

Wollman, A. J., Shashkova, S., Hedlund, E. G., Friemann, R., Hohmann, S., and Leake, M. C. (2017). Transcription factor clusters regulate genes in eukaryotic cells. *Elife* 6. doi:10.7554/eLife.27451.

Zawadzki, P., Stracy, M., Ginda, K., Zawadzka, K., Lesterlin, C., Kapanidis, A. N., et al. (2015). The Localization and Action of Topoisomerase IV in Escherichia coli Chromosome Segregation Is Coordinated by the SMC Complex, MukBEF. *Cell Rep.* 13, 2587–96. doi:10.1016/j.celrep.2015.11.034.

Figure 1 Schematic diagrams of high-speed narrowfield microscopy and the experimental system. (a) The imaging framework showing the bespoke fluorescence microscope and diagrams of image acquisition. (b) The structure of AF647 labeled CCL19 and CXCL13.

Figure 2 Single-molecule stoichiometry of CCL19-AF647. (a) Tracking of photoblinking AF647: localizations and intensity over time with sample images from the acquisition. (b) Distribution of apparent CCL19 foci stoichiometry (grey) overlaid with the predicted distribution based on randomly overlapping PSFs (blue). (c) Kernel density estimates of intensity of AF647 labeled CCL19 in collagen (solid blue line), and under heparan sulfate immobilization (solid black line); CXCL13 in collagen (dotted blue line), and under heparan sulfate immobilization (dotted black line); and BSA in 10% Ficoll (solid red line). All traces are normalized to the primary peak for clarity (see Supplementary Material).

Figure 3 Simulations of chemokine data. (a) Sample simulation images, shown with and without Gaussian white noise added. Scale bar 1 µm. (b) Two-gamma distribution fit (red) to diffusion coefficients found from a simulation of 1.6 and 10 $\mu m^2 s^{-1}$ data with Gaussian white noise. (c) Histograms showing the distribution of simulated 0 $\mu m^2 s^{-1}$ data with (red, overlaid) and without (blue) Gaussian white noise. (d) Diffusion coefficient distribution from a simulation of 0 and 9 $\mu m^2 s^{-1}$ data with Gaussian white noise. Fitted populations are shown in black for the immobile, red for the mobile and blue for the combined fit. Shaded areas indicate one standard deviation.

Figure 4 Comparing FRAP, FCS, and single molecule tracking on BSA-AF647 in 10% Ficoll 400. (a) Single-molecule tracking: Simplified schematic of the stages in tracking and the resulting fit with shaded regions indicating error bounds of one standard deviation. (b) FRAP: schematic of technique, profile of bleached region in an immobilized sample and example fluorescence intensity recovery trace. (c) FCS:

Schematic of the confocal volume, example section of intensity fluctuation trace and correlation curve.

Figure 5 Single particle tracking of chemokines in collagen. SHIM of collagen network in (a) 2D and (b) 3D. (c) Representative consecutive sub-millisecond images of chemokines in collagen. (d), (e) Fitted diffusion coefficient distribution of CXCL13-AF647 and CCL19-AF647 showing mobile and immobile components in a collagen matrix with (f) just the fitted high mobility diffusion coefficient distributions of CXCL13-AF647 (cyan) and CCL19-AF647 (magenta) (shaded areas indicate one standard deviation).

Figure 6 Confocal microscopy quantification of CXCL13-AF647 binding to lymph node follicles. (a) Schematic diagram of approximate locations of B cell follicles in a wild type murine lymph node. (b) Exemplar confocal microscopy images of CXCL13-AF647 and BSA-AF647 binding to lymph node tissue follicles (B220+ regions of lymph node tissue sections), and control with only B220 staining. (c) Quantification of the total fluorescent intensity for a fixed size imaging plane within a lymph node follicle. Each data point represents a distinct follicle.

Figure 7 Single molecule analysis of CXCL13-AF647 in tissue. (a) Intensity average image of image acquisition to show autofluorescent ECM in B220 stained B cell follicle with no added chemokine. (b) Areas of (a) identified as ECM by segmentation with overlaid track localizations colored orange. (c) Intensity average image of image acquisition to show autofluorescent ECM in B220 stained B cell follicle with added chemokine. (d) Areas of (c) identified as ECM by segmentation with overlaid track localizations colored by location on ECM (blue) or in the interstitial spaces between cells (cyan). (e) Comparison of diffusion coefficients of localisations in ECM locations in the presence (blue) and absence (orange) of CXCL13-AF647 (f) Comparison of diffusion coefficients for the ECM (blue) and chemokine (cyan) populations when tracking CXCL13-AF647 in lymph node tissue shown. (g) Distribution and fit of chemokine diffusion coefficients of CXC13-AF647 in tissue sections, shaded area indicates one standard deviation.

Simulated condition	**Number of Tracks**	**Fitted value of D ($\mu m^2 s^{-1}$)**	**Fitted value of N ($\mu m^2 s^{-1}$)**	***R^2* value of fit**
1.6 $\mu m^2 s^{-1}$, no noise	1,579	1.72 (1.68, 1.76)	2.24 (2.15, 2.33)	0.9892
1.6 $\mu m^2 s^{-1}$, noise	401	2.19 (2.12, 2.25)	1.75 (1.67, 1.83)	0.9777
10 $\mu m^2 s^{-1}$, no noise	1,519	10.21 (9.77, 10.6)	2.27 (2.08, 2.45)	0.9343
10 $\mu m^2 s^{-1}$, noise	463	10.04 (9.53, 10.54)	2.77 (2.47,3.08)	0.8968

Table 1 Results of one gamma distribution fitting to simulated single diffusion coefficient distributions. Noise or no noise refers to the presence of Gaussian white noise proportional to the intensity in the simulation. 95% confidence intervals are given in brackets.

Condition	**Diffusion coefficient ($\mu m^2 s^{-1}$)**	**Number of measurements**
Theoretical with Stokes radius 3.48nm	12.3 ±0.1	
FCS	18.8 ±0.3	27 traces
FRAP	7.1 ±0.3	30 repeats
Single-molecule tracking	9.3 ±0.4	2,608 tracks (fitted 1,113 mobile tracks)

Table 2 Measurements of the diffusion coefficient of Alexa-647 labeled BSA in 10% Ficoll 400. Variation on the theoretical value is due to a potential ± 2°C temperature change in the laboratory.

AF647 labelled chemokine	**Theoretical diffusion coefficients in water ($\mu m^2 s^{-1}$)**	**Fitted diffusion coefficient ($\mu m^2 s^{-1}$)**	**Error ($\mu m^2 s^{-1}$)**	**Number of highly mobile tracks**	**R^2 of combined fit**
CXCL13	149	6.2	0.3	1,930	0.980
CCL19	146	8.4	0.2	4,859	0.984

Table 3 Diffusion coefficients of CXCL13 and CCL19 in collagen. Optimized values were found by fitting a two gamma distribution to single molecule tracking data.

Figure 1.TIF

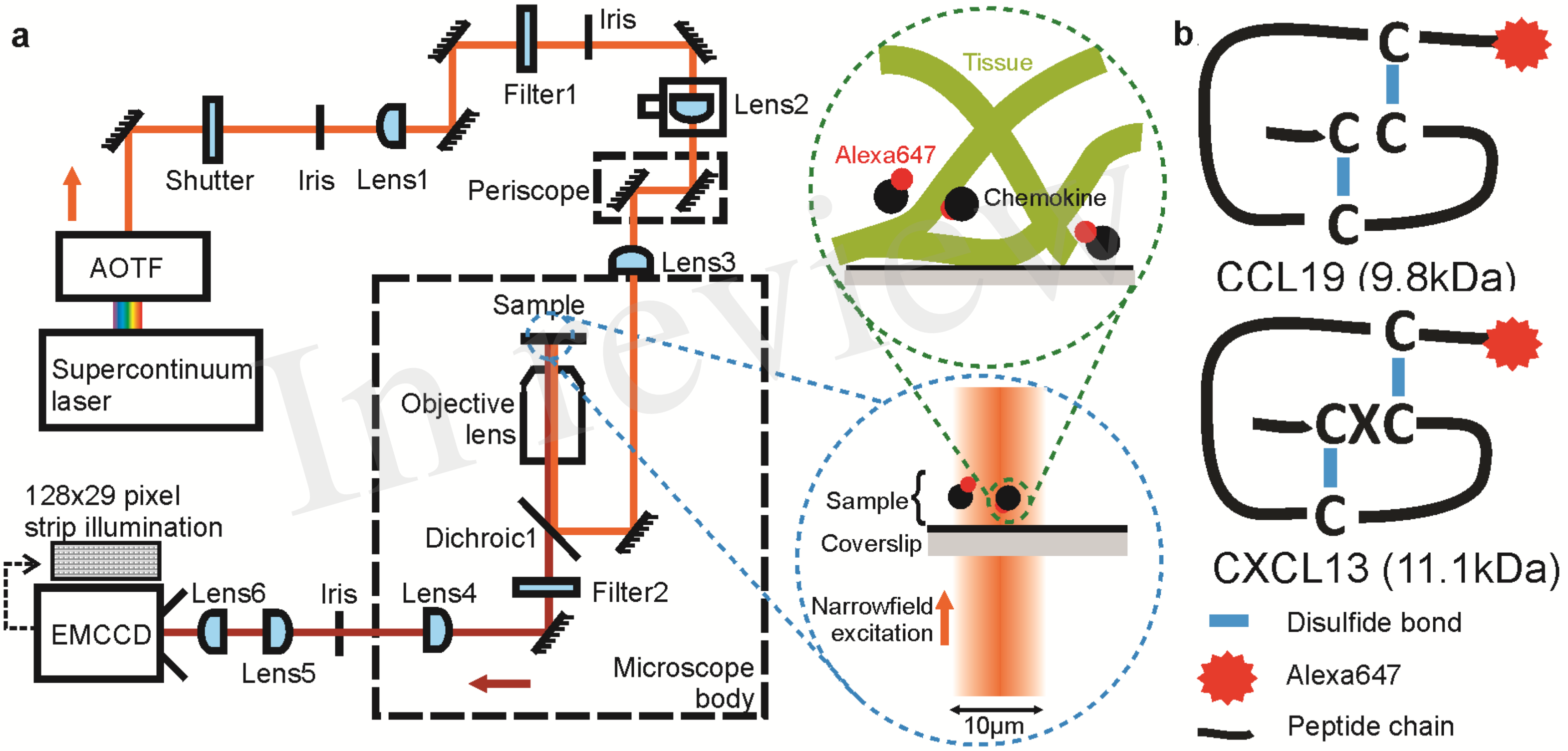
a
Iris
Filter1
Lens2
Shutter
Iris
Lens1
Periscope
AOTF
Supercontinuum laser
Lens3
Sample
Objective lens
128x29 pixel strip illumination
Dichroic1
Filter2
Lens6
Iris
Lens4
EMCCD
Lens5
Microscope body
Tissue
Alexa647
Chemokine
Sample
Coverslip
Narrowfield excitation
10µm
b
C
C C
C
CCL19 (9.8kDa)
C
CXC
C
CXCL13 (11.1kDa)
Disulfide bond
Alexa647
Peptide chain

Figure 2.TIF

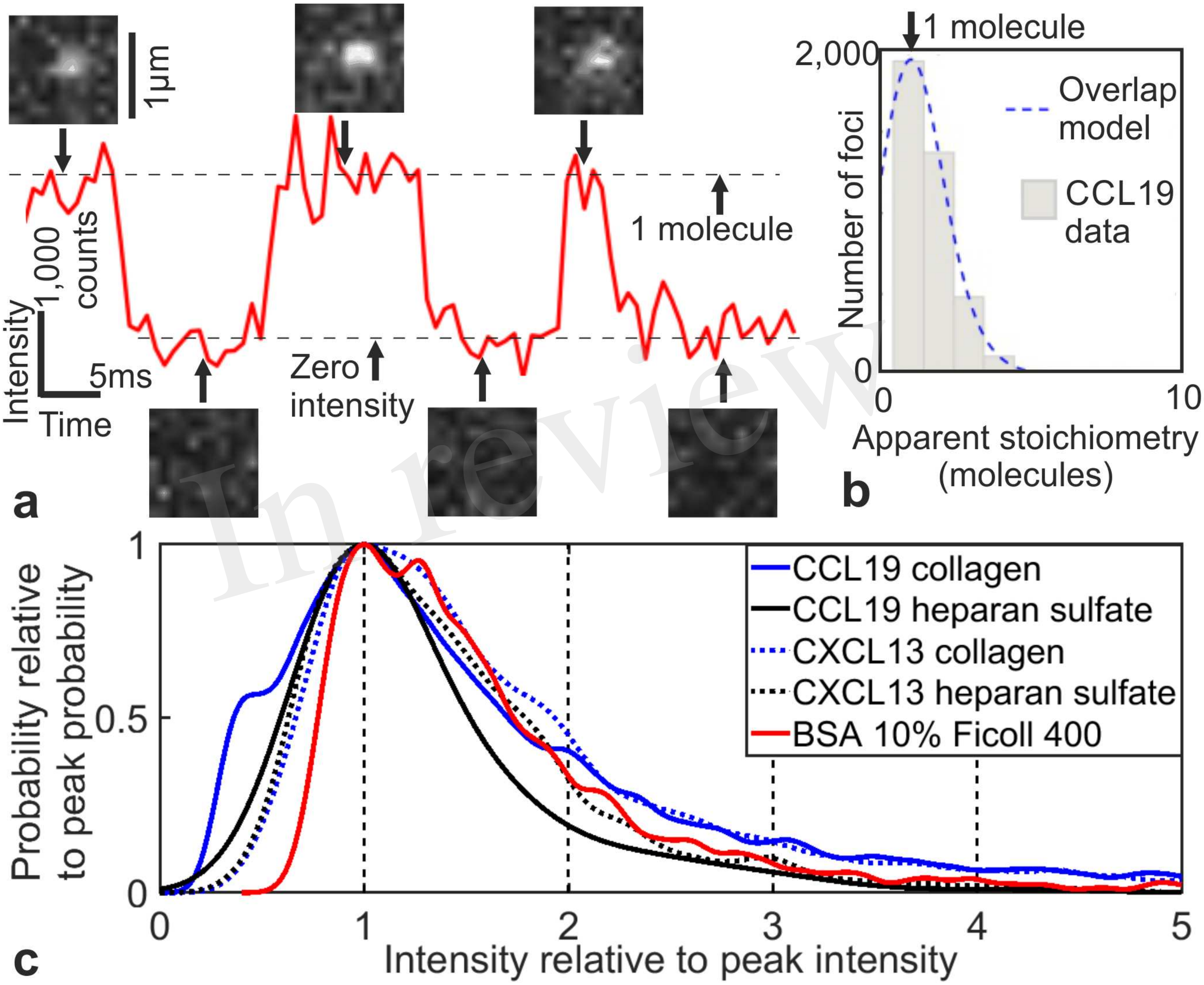
1µm
1 molecule
Zero intensity
Intensity 1,000 counts
Time 5ms
a
1 molecule
2,000
0
Number of foci
Overlap model
CCL19 data
0
10
Apparent stoichiometry (molecules)
b
Probability relative to peak probability
1
0.5
0
CCL19 collagen
CCL19 heparan sulfate
CXCL13 collagen
CXCL13 heparan sulfate
BSA 10% Ficoll 400
0
1
2
3
4
5
Intensity relative to peak intensity
c

Figure 3.TIF

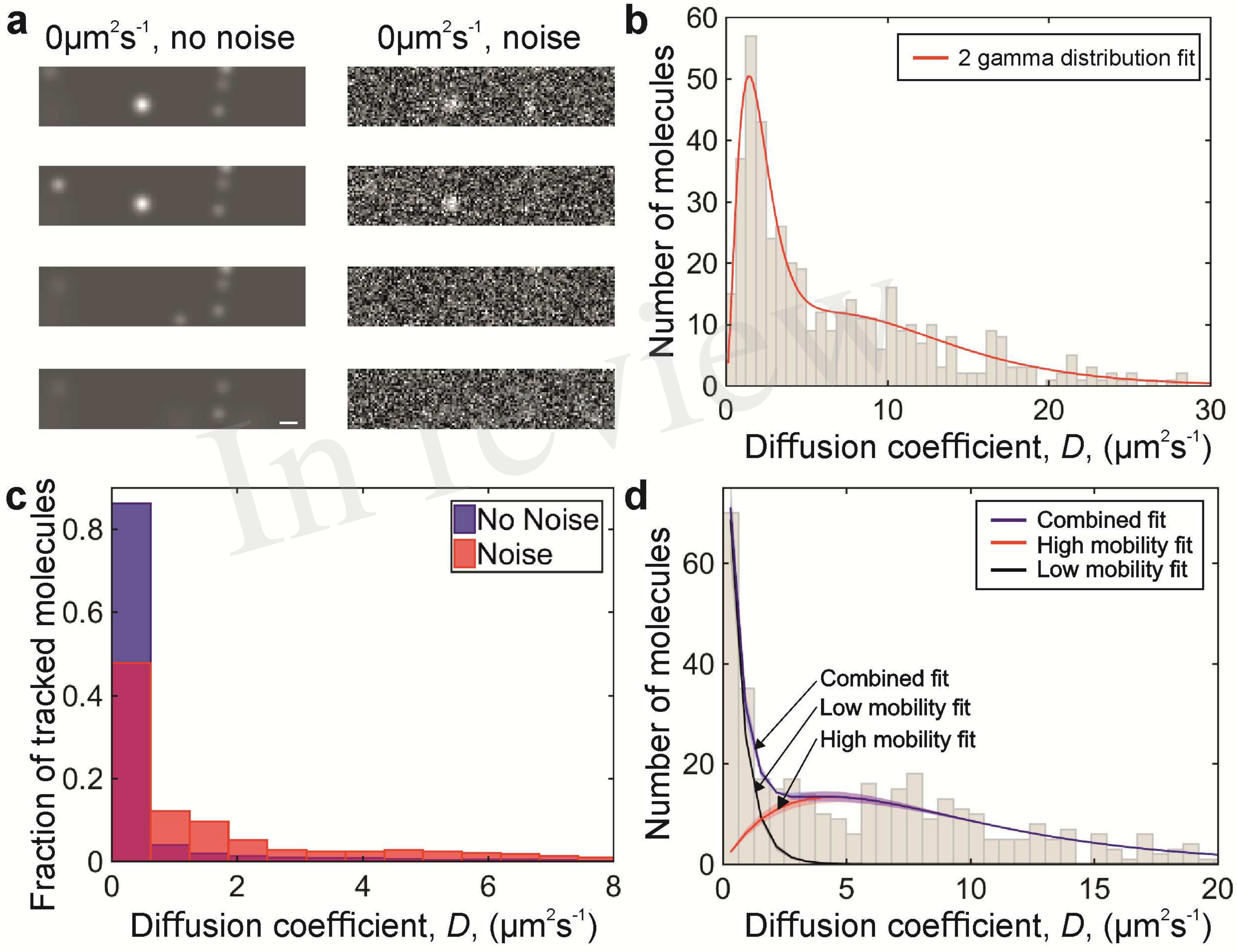
a
0μm^{2}s^{-1}, no noise
0μm^{2}s^{-1}, noise
b
2 gamma distribution fit
Number of molecules
0
10
20
30
40
50
60
0
10
20
30
Diffusion coefficient, D, (μm^{2}s^{-1})
c
No Noise
Noise
Fraction of tracked molecules
0
0.2
0.4
0.6
0.8
0
2
4
6
8
Diffusion coefficient, D, (μm^{2}s^{-1})
d
Combined fit
High mobility fit
Low mobility fit
Combined fit
Low mobility fit
High mobility fit
Number of molecules
0
20
40
60
0
5
10
15
20
Diffusion coefficient, D, (μm^{2}s^{-1})

Figure 4.TIF

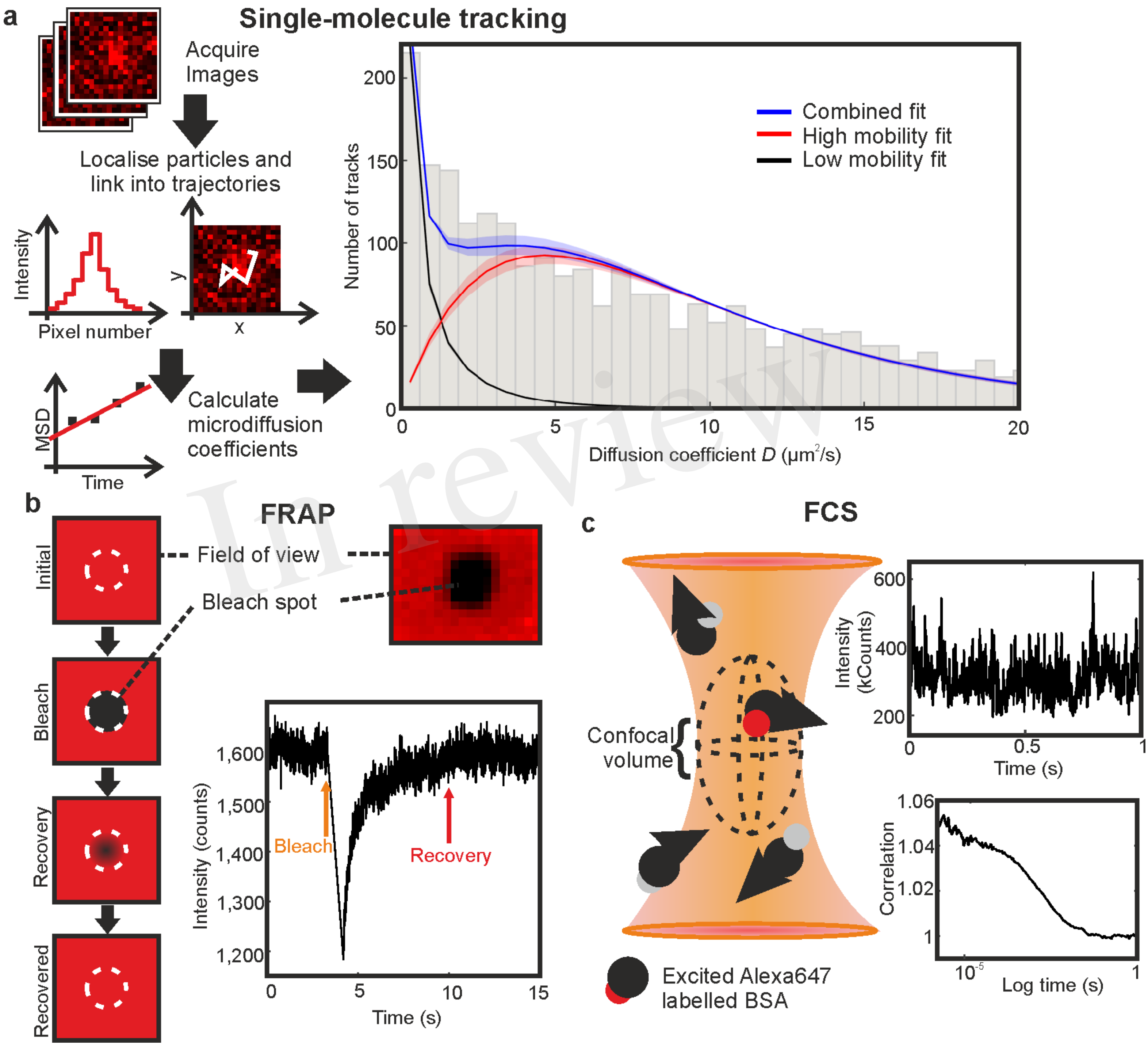
a
Single-molecule tracking
Acquire Images
Localise particles and link into trajectories
Intensity
Pixel number
y
x
MSD
Time
Calculate microdiffusion coefficients
Combined fit
High mobility fit
Low mobility fit
Number of tracks
200
150
100
50
0
0
5
10
15
20
Diffusion coefficient D (μm²/s)
b
FRAP
Initial
Bleach
Recovery
Recovered
Field of view
Bleach spot
Intensity (counts)
1,600
1,500
1,400
1,300
1,200
Bleach
Recovery
0
5
10
15
Time (s)
c
FCS
Confocal volume
Excited Alexa647 labelled BSA
Intensity (kCounts)
600
400
200
0
0.5
1
Time (s)
Correlation
1.06
1.04
1.02
1
10⁻⁵
1
Log time (s)

Figure 5.TIF

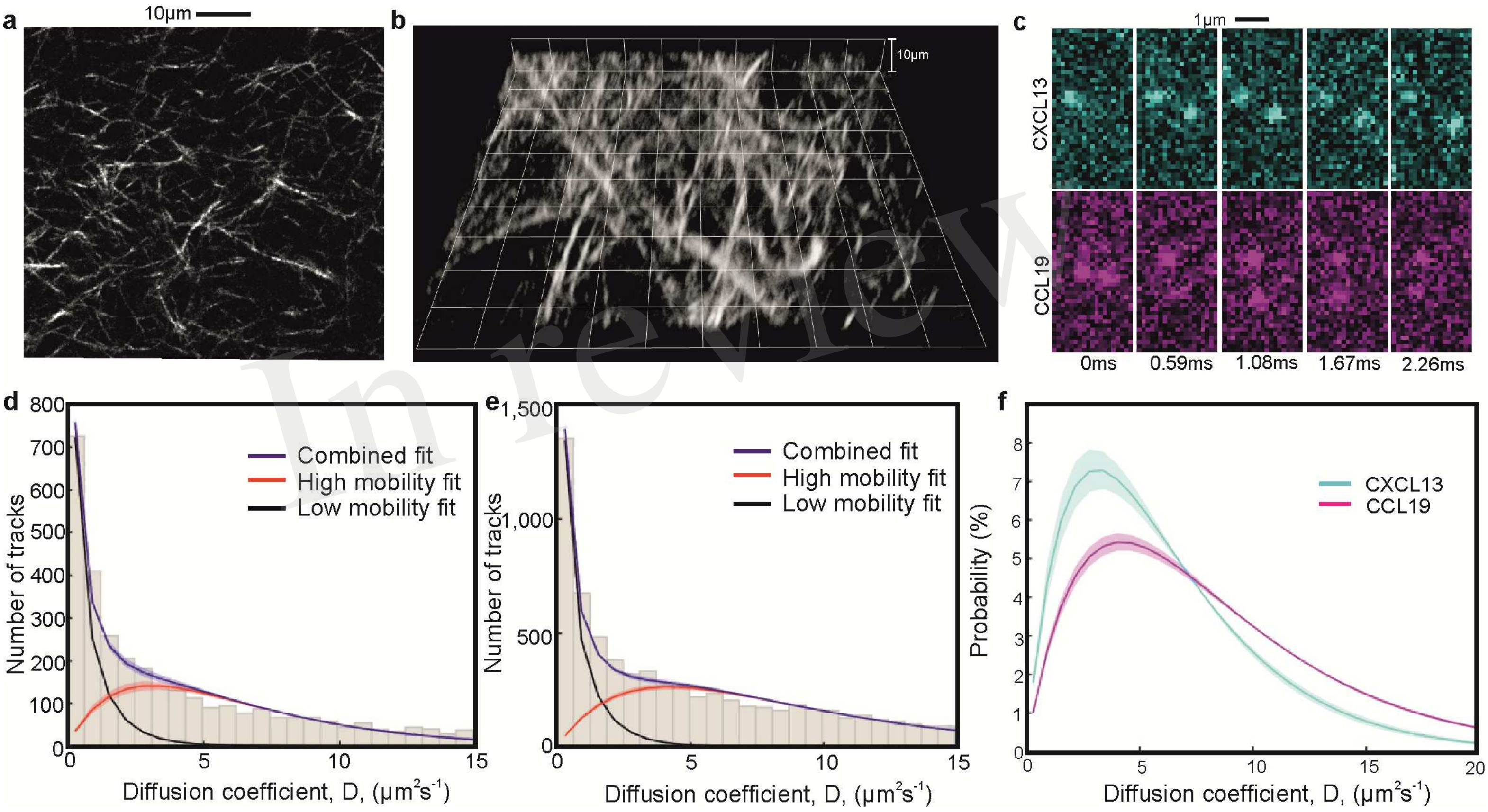
a
10μm
b
10μm
c
1μm
CXCL13
CCL19
0ms
0.59ms
1.08ms
1.67ms
2.26ms
d
Number of tracks
800
700
600
500
400
300
200
100
0
Combined fit
High mobility fit
Low mobility fit
0
5
10
15
Diffusion coefficient, D, (μm²s⁻¹)
e
Number of tracks
1,500
1,000
500
0
Combined fit
High mobility fit
Low mobility fit
0
5
10
15
Diffusion coefficient, D, (μm²s⁻¹)
f
Probability (%)
8
7
6
5
4
3
2
1
0
CXCL13
CCL19
0
5
10
15
20
Diffusion coefficient, D, (μm²s⁻¹)

Figure 6.TIF

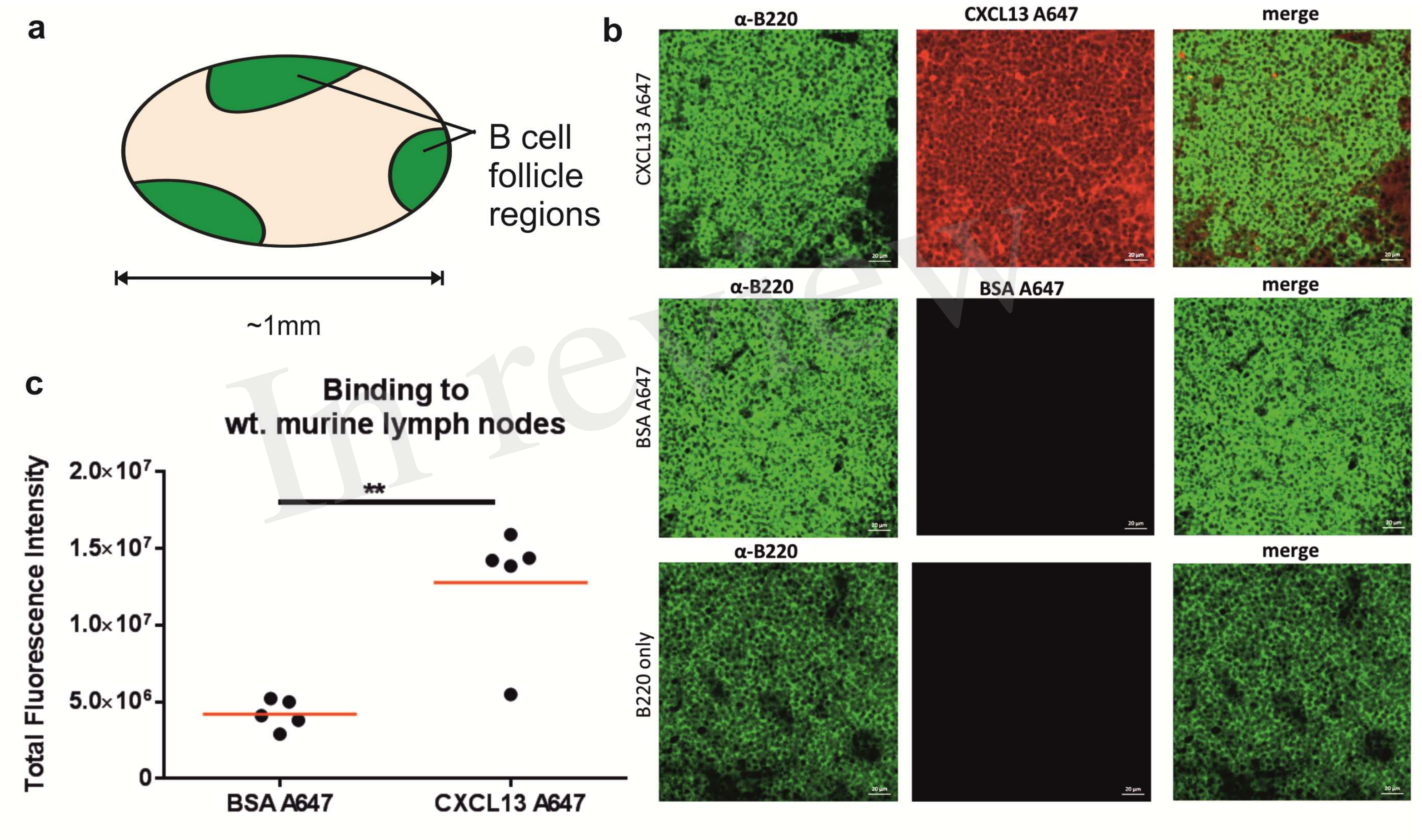

a
B cell follicle regions
~1mm
b
α-B220
CXCL13 A647
merge
CXCL13 A647
α-B220
BSA A647
merge
BSA A647
α-B220
merge
B220 only
20 µm
c
Binding to wt. murine lymph nodes
Total Fluorescence Intensity
2.0×10⁷
1.5×10⁷
1.0×10⁷
5.0×10⁶
0
**
BSA A647
CXCL13 A647

Figure 7.TIF

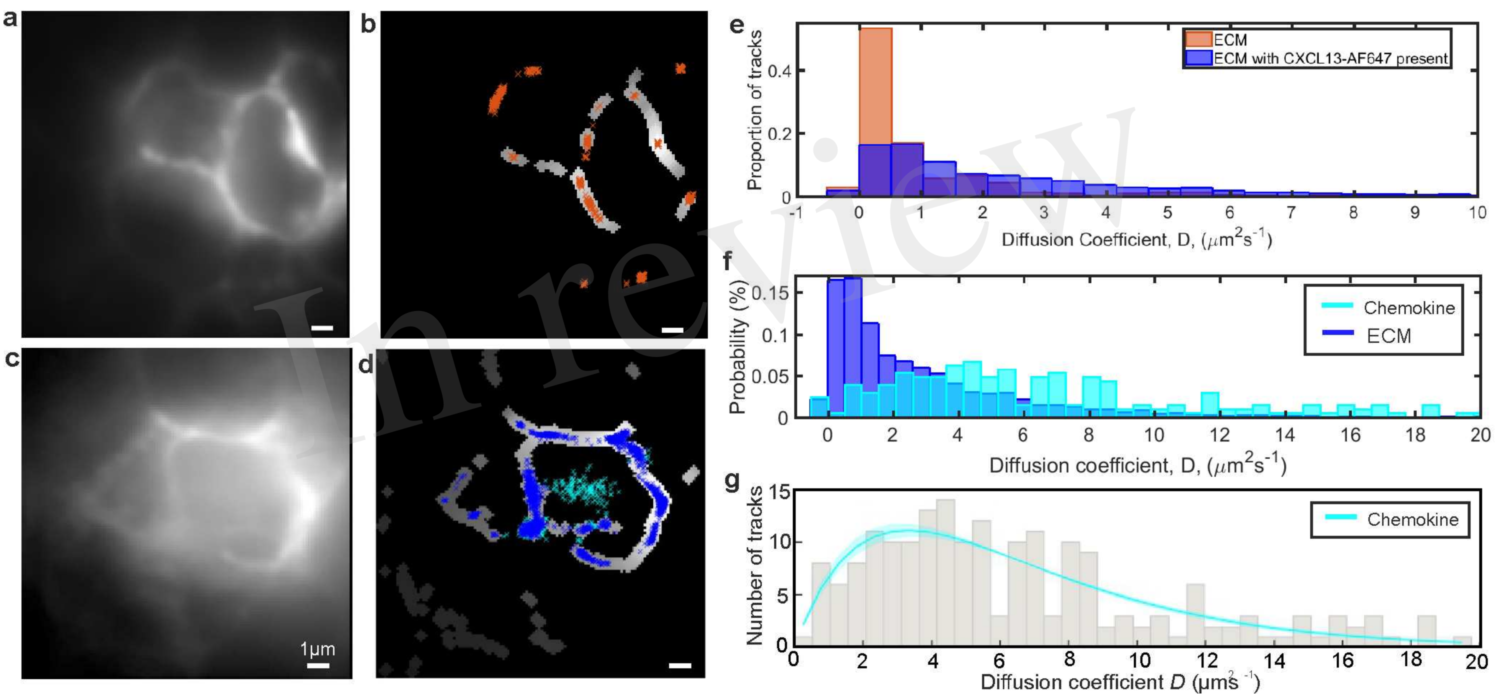
a
b
c
1µm
d
e
Proportion of tracks
0
0.2
0.4
ECM
ECM with CXCL13-AF647 present
-1 0 1 2 3 4 5 6 7 8 9 10
Diffusion Coefficient, D, (μm^{2}s^{-1})
f
Probability (%)
0
0.05
0.1
0.15
Chemokine
ECM
0 2 4 6 8 10 12 14 16 18 20
Diffusion coefficient, D, (μm^{2}s^{-1})
g
Number of tracks
0
5
10
15
Chemokine
0 2 4 6 8 10 12 14 16 18 20
Diffusion coefficient D (µm^{2}s^{-1})